Prediction of Crystallographic Texture Evolution and Anisotropic Stress-strain Response during Large Plastic Deformation in α-Titanium Alloys

A Thesis

Submitted to the Faculty

of

Drexel University

by

Xianping Wu

in partial fulfillment of the

requirements for the degree

of

Doctor of Philosophy

September 2006

Dedications

This thesis is dedicated to my parents, Chenghao Wu and Mingmei Wu.

Acknowledgements

I would like to express my sincere gratitude for everyone who helped and supported me during my study towards Ph.D. degree. In particular, I would like to thank:

- My advisors: Dr. Surya R. Kalidindi and Dr. Roger D. Doherty, Drexel University. They not only shared their knowledge with me throughout my four years at Drexel, but also enhanced my life in personal level. Without their constant encouragement, advice and financial support, this work would not be possible.
- My committee members: Dr. David Fullwood, Dr. Jonathan Spanier, Dr. Alan Lau from Drexel University, and Dr. Joshua R. Houskamp from Oak Ridge Associated Universities at Army Research Laboratory, for their input and advice to my study.
- Dr. Christopher Li, Dr. Frank Ko and Dr. Antonios Zavaliangos for their discussion and advice during my graduate seminar, candidacy exam and pre-defense.
- Dr. Ayman A. Salem and Dr. Carl Necker for providing the experimental measurements used in my study.
- My colleagues at MMG group: Mr. Hari Duvvuru, Mr. Massimiliano Binci, Mr. Dejan Stojakovic, Mr. Christopher Hovanec, Mr. Siddhartha Pathak, Mr. Marko Knezevic, Mr. Brendan Donohue, Mr. Tony Fast, Ms. Melanie Patel and Ms. Naomi Barth for their help in various aspects of my work..
- Dr. Gwénaëlle Proust and Dr. Joshua R. Houskamp for their help and advice on my academic and personal life during my first three years at Drexel.

- Mrs. Judy Trachtman, Ms. Dorilona Rose, and Ms. Crystal White for their help on all administrative matters and being so friendly with students.
- All faculty and staff members at Department of Materials Science and Engineering, for establishing such a nice environment, which made my study at Drexel rewarding.
- My fellow graduate students at Department of Materials Science and Engineering, for being so supported and friendly, which made my life at Drexel enjoyable.

Table of Contents

List of Tables

List of Figures

Abstract

Prediction of Crystallographic Texture Evolution and Anisotropic Stress-strain Response during Large Plastic Deformation in α-Titanium Alloys

Xianping Wu

Prof. Surya R. Kalidindi

Prof. Roger D. Doherty

A new Taylor-type polycrystalline model has been developed to simulate the evolution of crystallographic texture and the anisotropic stress-strain response during large plastic deformation in α-titanium alloys at room temperature. Crystallographic slip, deformation twinning, and slip inside twinned regions were all considered as contributing mechanisms for the plastic strain in the model. This was accomplished by treating the dominant twin systems in a given crystal as independent grains once the total twin volume fraction in that crystal reached a predetermined saturation value. The newly formed grains were allowed to independently undergo further slip and the concomitant lattice rotation, but further twinning was prohibited. New descriptions have been established for slip and twin hardening and the complex coupling between them. Good predictions were obtained for the overall anisotropic stress-strain response and texture evolution in several different monotonic deformation paths on annealed, initially textured samples of two different chemical compositions of α-titanium alloys.

The polycrystalline plasticity model presented here is built on the Taylor assumption of uniform deformation gradient in all of the constituent grains. The effects of this gross simplification have been evaluated by comparing the predicted stress and strain distributions between Taylor model and the more sophisticated finite element models that relax the assumption of the uniform strain. The anisotropy of the plastic behavior was

observed to strongly influence the deviation of the Taylor model predictions from the finite element model predictions when comparing the stress and strain distributions in deformed polycrystalline α-titanium with initially random texture.

The slip parameters established using the crystal plasticity model developed here were utilized in a novel spectral framework, called Microstructure Sensitive Design (MSD), for constructing elastic-plastic property closures in hexagonal polycrystals. The main focus was on the influence of the crystallographic texture (in the hcp polycrystals) on the components of the macroscale anisotropic elastic stiffness, macroscale anisotropic tensile yield, and the macroscale R-ratios (ratio of the transverse strains in tensile deformation mode) exhibited by the material.

CHAPTER 1: INTRODUCTION

Titanium and its alloys constitute an important class of metals with numerous applications in the defense, aerospace, biomedical and construction industries due to their outstanding properties such as low density, high strength, and excellent corrosion resistance [1-3]. Understanding the mechanical behavior of these materials during thermo-mechanical processes is crucial to control the properties of the final products. Like most hexagonal close-packed metals, α-titanium is characterized by the high mechanical anisotropy at ambient temperature. Earlier studies on deformation behavior of α-titanium showed that plastic deformation is accommodated by a complex mixture of crystallographic slip and deformation twinning [4-8]. It is commonly agreed that prismatic slip along <*a*> is the most favorable slip family in pure titanium at ambient temperature because the hcp structure of pure titanium has less-than-ideal *c*/*a* ratio of 1.587. Basal <*a*> and pyramidal <*a*> are the other two possible slip families. However, above deformation modes together only provide four independent slip systems whereas five independent slip systems are required for a polycrystalline material to accommodate an arbitrary plastic deformation [9]. Consequently, pyramidal <c+a> or deformation twinning are necessary to be activated during plastic deformation [9, 10].

The fact that α-titanium undergoes both slip and twinning during plastic deformation makes it difficult to identify the role played by different deformation mechanisms on the overall mechanical behavior. Many studies have reported the occurrence of deformation twinning in pure titanium and conducted numerous investigations on the role played by twinning in both strain hardening response and

texture evolution [7, 11, 12]. In a recent work, for example, three distinct stages of the strain-hardening response of pure titanium during compression testing at ambient temperature were reported [13]. The first stage with a falling strain-hardening rate was associated with the absence of twinning, the second stage with an increasing strain-hardening rate was attributed to the increase of twin volume fraction, and the third stage with a falling strain-hardening rate was coincident with the saturation of twin volume fraction. In a more recent paper [8], the physical insights behind the correlation of the strain-hardening rate and twin volume fraction were interpreted by the two competing effects of deformation twinning on the overall strain-hardening response: (1) strain hardening via the Hall-Petch mechanism (i.e., a reduction in the effective slip length) and the Basinski mechanism (i.e., a trapping of sessile dislocations inside twins), and (2) texture softening due to a reorientation of the twinned regions to softer orientations. These experimental observation and hypotheses could be considered as significant advances in understanding the role of deformation twinning in strain hardening behavior of hcp materials.

Although the exact mechanisms by which twins influenced the overall strain hardening response in pure titanium are still not fully understood, earlier studies have provided convincing arguments for the need to include deformation twinning as an important contributor in accommodating a significant portion of the imposed plastic deformation at ambient temperature. Specifically, a large volume fraction (e.g. 40%) of the moderately deformed material in the compression tests of polycrystalline α-titanium at room temperature was occupied by deformation twins [8, 13]. These twins are thick enough to permit slip inside twinning. Therefore, crystallographic slip, deformation

twinning and slip inside twins should all be considered as possible plastic deformation mechanisms in pure titanium at ambient temperature.

A number of modeling techniques have been used in literature to simulate the development of texture in deformation processes and the associated evolution of properties in metallic polycrystals. Among these modeling techniques, crystal plasticity model was considered to provide more accurate simulations of deformation processes by taking into account explicitly the details of physics and geometry of deformation at crystal level. One of the major successes of the crystal plasticity theory has been the ability to predict both the anisotropic stress-strain response of metals as well as the evolution of the averaged crystallographic texture in a variety of large deformation paths.

The crystal plasticity models have been demonstrated to be fairly accurate for cubic polycrystalline metals, in which plastic deformation occurred predominantly by slip [14-18]. Over the last ten years, the application of crystal plasticity models to hexagonal close-packed metals has received substantial attention [19-21]. Recently, a rigorous framework was developed for materials that deform by both slip and twinning [22] and a quantitative description of slip-twin hardening was proposed [23]. However, numerical implementation of theses schemes is quite cumbersome when slip inside the twinned regions is to be allowed as a significant contribution to the plastic deformation in the crystal. In the current work, a novel modeling framework was proposed to overcome the above obstacle by using the grain-fragmentation scheme. In addition, the previous version of slip-twin hardening functions has been further expanded by allowing different hardening parameters for different slip and twin families. Furthermore, this new

framework has been successfully applied to two different compositions of α-titanium (two different purity levels).

It is important to note that the Taylor assumption was used to achieve polycrystalline response from individual crystals in the proposed framework. Consequently, some of the discrepancy between the prediction and measurement can be attributed to this gross simplification. In order to evaluate the effects of the Taylor assumption, the predicted stress and strain distributions over a random-textured polycrystal were compared with the results from a finite element framework as a function of plastic anisotropy.

Taylor-type crystal plasticity models are usually used to predict the texture evolution and the stress-strain response providing the initial texture and deformation paths are known. In the actual design tasks, however, designers are very often faced with inverse problems where designers need to know in advance all the possible mechanical properties of a given material system before they optimize their design. A novel mathematical framework called Microstructure Sensitive Design (MSD) [24-26] was recently formulated to address this need. MSD can be very useful in delineating property closures [27] that identify the complete set of theoretically feasible combinations of macroscale (homogenized) properties in a given material system. This framework has been successfully applied previously to cubic polycrystals assuming crystallographic texture is the dominant influence on the macroscale properties of interest [26, 28]. The same method becomes extremely difficult when applied to hcp polycrystals. In this thesis, a new computational scheme was reported for delineating elastic-plastic closures for hcp polycrystals using the spectral framework of MSD.

This thesis is organized as follows. Chapter 2 presents the new modeling framework and the associated strain hardening functions. Chapter 3 describes the procedure for calibrating the proposed crystal plasticity model. This new modeling framework with established parameters is evaluated by direct comparison with experimental measurements. The effects of the Taylor assumption are evaluated by comparing the predicted stress and strain distributions in polycrystals by both the Taylor-type model and the finite element model. Chapter 4 explains the methodology to delineate the elastic-plastic property closures for hcp polycrystals using MSD framework. A variety of comprehensive property closures are depicted in this chapter. Conclusions and future work are presented in chapter 5.

CHAPTER2: MODELING TEXTURE EVOLUTION AND ANISOTROPIC STRESS-STRAIN RESPONSE USING A TAYLOR-TYPE MODEL

2.1. Introduction

A rigorous formulation of the elastic-plastic constitutive relations for crystalline materials undergoing finite plastic strains by crystallographic slip alone is now well established in literature [14, 15, 17]. However, many materials exhibit deformation twinning as an additional mode of plastic deformation, especially at low homologous temperatures and/or high strain rates [10, 29, 30]. Several studies have reported extensive deformation twinning in room (and lower) temperature deformation of α-Ti [4, 6, 8]. Consequently, it is highly desirable to extend the current crystal plasticity models to include deformation twinning as an additional mode of plastic deformation. The main obstacle in accomplishing this goal is the lack of an efficient method to handle the extremely large number of new orientations created by deformation twinning. Three different approaches have been proposed in the literature to address this problem:

(1.) Predominant Twin Reorientation (PTR) Method: This method was originally proposed by Van Houtte [31] and improvements were made by Tome et al. [32]. Staroselsky and Anand [33, 34] have formulated a rigorous and efficient numerical approach for the use of rate-independent crystal plasticity theories and applied it with the PTR model to study stress-strain responses and texture evolution in low stacking fault energy cubic and hexagonal metals. Kaschner et al. [35] employed the PTR method in a visco-plastic self-consistent crystal plasticity modeling framework to study the role of twinning in the hardening response of zirconium during temperature reloads. In the PTR scheme, twinning is essentially treated as a pseudo-slip mechanism while the evolution of

the volume fractions of the twinned regions is carefully tracked in each grain. Consequently, the twinned regions are not reoriented at the end of each time step. Instead, a statistical criterion is devised and employed to ensure that an appropriate number of heavily twinned grains are completely reoriented into their predominant twin orientations; this number is selected based on the total volume fraction of twinned regions in the entire polycrystal. A major advantage of this method is that the number of total grain orientations remains constant during the entire simulation. The disadvantage of this method is that it can not be applied at the single crystal level and is not particularly amenable to the highly efficient, total Lagrangian, fully implicit time integration procedure developed recently for the crystal plasticity constitutive framework [15].

(2.) Volume Fraction Transfer (VFT) Scheme: This approach was proposed by Tome et al. [32] and employs weighted (and binned) grain orientations to address the problem of tracking the large number of new orientations created by deformation twinning. In this scheme, the relevant Euler space of distinct grain orientations (also called the fundamental zone of orientations [36]) is suitably binned and the texture in the sample is represented by the weights associated with the binned orientations. Therefore, only the weights of the grain orientations need to be suitably modified to reflect the orientation changes caused by twinning, and hence there is no need to create new orientations. However, the disadvantages of this method are that a very large number of bins are needed (especially for the lower symmetry hexagonal metals) and that this approach is also not particularly amenable for implementation of the efficient fully implicit time integration procedure developed recently for the crystal plasticity constitutive framework.

(3.) Total Lagrangian Approach: Building on a total Lagrangian crystal plasticity framework that was initially formulated for materials that exhibit only crystallographic slip, Kalidindi [22] proposed a new interpretation of the multiplicative decomposition of the total deformation gradient into its elastic and plastic components when deformation twinning is added as an additional mode of plastic deformation. The main advantages of this method are that it allows the application of the crystal plasticity theory with deformation twinning to a single crystal while taking full advantage of the efficient fully implicit time integration schemes that have been previously developed and validated. The disadvantage of this method continues to be the fact that the numerical implementation of the scheme is quite cumbersome when slip inside the twinned regions is to be allowed as a significant contribution to the plastic deformation in the crystal. The importance of including slip inside twins as an additional mode of plastic deformation was established in a recent experimental study [8, 13], where it was observed that the averaged Taylor factor for the twinned regions in a sample of high purity α-Ti deformed in simple compression was about 40% lower than that for the matrix regions, implying that the slip inside the twinned regions would be a significant component of the overall plastic deformation in this sample. In the prior modeling effort for low stacking fault energy fcc metals, the fact that the potential twin systems in the very thin twins are co-planar with the potential slip systems made it relatively easy to incorporate slip inside twinning as a contribution to the overall plastic deformation [37]. However, the potential twin systems in hcp metals are non-coplanar with all of the potential slip systems, and therefore tracking the slip activity inside the already formed twins becomes quite cumbersome in this approach.

It is therefore clear that there exist a number of outstanding problems in the incorporation of deformation twinning and, slip inside deformation twins in the current crystal plasticity modeling framework. Recent experimental studies have provided several new insights that, in turn, suggest new simplifying approximations to overcome some of the difficulties described above in the modeling efforts. Of particular importance to the work presented here is the observation reported by Salem et al. [8] that much of the deformation twinning in high purity α-Ti deformed in simple compression at room temperature occurred in a relatively narrow moderate strain range of 0.05 to 0.3 (with most of the profuse twinning actually occurring in an even narrower strain range of 0.15-0.20). At higher strain levels, the grain structure fragmented substantially and the rate of deformation twinning decreased dramatically. Although the precise reason for the saturation of twinning activity at high strains is not yet fully understood, it is generally attributed to the much higher stresses required to produce the shorter deformation twins in the smaller fragmented grains [13, 30].

The main objective of the work presented in this chapter is to report on the latest effort to develop an improved Taylor-type crystal plasticity model for α-Ti hcp polycrystals. This new model employs a grain fragmentation concept. In this new model, following the earlier approaches [23, 31], deformation twinning is initially treated as a pseudo-slip mechanism. When a certain volume fraction of any grain has undergone deformation twinning that particular grain is fragmented into its dominant twin systems. During subsequent deformation, neither the parent grain nor any of its newly formed fragmented components (i.e. twins) are allowed to produce further twins. The main motivation for exploring this approach stems from the previously described observations

in α-Ti where it was noted that deformation twinning dominates the texture evolution in the polycrystal in a short intermediate strain regime. Therefore, the underlying approximations in the proposed approach should have very little effect on the texture evolution of the polycrystal at large strains. Furthermore, since the grain is allowed to fragment only once and only into its dominant twin components, the number of new grains produced is relatively small and can be efficiently handled with only a moderate increase in the computational effort. Finally, the proposed approach can be easily implemented in the previously established, numerically efficient, total Lagrangian framework with the associated fully implicit time integration procedure. In many ways, the proposed approach here combines the best aspects of the different modeling approaches described earlier [22, 31, 32]. In addition, the slip-twin hardening functions have been expanded from the previously used versions [23], and have been observed to provide better predictions of the anisotropic stress-strain responses.

2.2. Modeling Framework

A new Taylor-type crystal plasticity model is presented here for room temperature deformation of high purity α-Ti using a notation that is now standard in this field [38]. In this notation, **F** represents the deformation gradient tensor, **L** represents the velocity gradient tensor, and **T** represents the Cauchy stress tensor. An important feature of the model presented here is the introduction of a grain fragmentation event based on the accumulated deformation twinning activity in the crystal. The details of the grain fragmentation event and the behavior of the grain prior and subsequent to this fragmentation event are described next.

2.2.1 *Grains Prior to Fragmentation*

The grains prior to fragmentation are modeled using essentially the approach described previously by Kalidindi [22], with some modifications in the strain hardening descriptions. The imposed total deformation gradient tensor on the crystal is multiplicatively decomposed into two components (see Figure 1):

$$\mathbf{F} = \mathbf{F}^{*}\mathbf{F}^{p}. \tag{2.1}$$

In this model, $\mathbf{F}^{p}$ denotes the plastic deformation gradient tensor that describes the overall (effective) shape change induced in the grain as a consequence of the crystallographic slip and deformation twinning in the grain, while $\mathbf{F}^{*}$ denotes the additional transformation (including elastic stretch and rotations) needed to account for the total imposed shape change induced by **F.** It is further assumed that the slip processes leave the lattice orientation unchanged, while deformation twinning rotates the lattice into a priori defined orientation (for the hexagonal crystals of interest in this study this relationship is conveniently described as a 180 degree rotation about the twin plane normal [10]). Consequently, the orientations of the twinned and untwined regions of the grain in the hypothetical intermediate configuration shown in Figure 1 (after the application of $\mathbf{F}^{p}$) are fully known a priori, given the initial orientation of the grain. The polar decomposition of $\mathbf{F}^{*}$ provides the elastic stretch and the overall lattice rotation between the intermediate configuration and the deformed configuration. In Figure 1, only one twin system is shown for clarity. However, multiple twin systems are allowed in one grain. Furthermore, the twinned region belonging to one twin system is idealized as a continuous block, while in reality, deformation twins occur as multiple plates. This

simplification was motivated by the reported experimental observations in literature [13, 39], which suggest that the deformation twins of a particular twin system occur as roughly parallel plates of similar lattice orientation. The fact that the twins of a single twin system occur as multiple plates does have a major influence on the hardening response of the crystal, and this aspect will be treated in section 2.3 using appropriate phenomenological slip and twin hardening laws.

The constitutive equation for the elastic response of a single crystal is expressed as

$$\mathbf{T}^* = \mathbf{C}\left[\mathbf{E}^*\right], \tag{2.2}$$

in which $\mathbf{C}$ represents the fourth-order anisotropic elasticity tensor, $\mathbf{T}^*$ and $\mathbf{E}^*$ are a pair of work conjugate stress and strain measures defined as

$$\mathbf{T}^* = \mathbf{F}^{*-1}\{(\det\mathbf{F}^*)\mathbf{T}\}\mathbf{F}^{*-T} \quad , \tag{2.3}$$

$$\mathbf{E}^* = \frac{1}{2}\{\mathbf{F}^{*T}\mathbf{F}^* - 1\}. \tag{2.4}$$

The evolution of plastic deformation gradient can be expressed as

$$\dot{\mathbf{F}}^{\mathrm{p}} = \mathbf{L}^{\mathrm{p}}\mathbf{F}^{\mathrm{p}}, \tag{2.5}$$

in which $\mathbf{L}^{\mathrm{p}}$ is plastic velocity gradient tensor expressed as

$$\mathbf{L}^{\mathrm{p}} = \sum_{\alpha}^{N^s} \dot{\gamma}^{\alpha}\mathbf{S}_o^{\alpha} + \sum_{\beta}^{N^{tw}} \dot{f}^{\beta}\gamma_{tw}^{\beta}\mathbf{S}_o^{\beta}. \tag{2.6}$$

The two terms on the right hand side of Eq. (2.6) represent the contributions to plastic deformation by slip and deformation twinning respectively. $\mathbf{S}$ denotes the unit slip (twin) tensor, defined as the dyadic product of two orthogonal unit vectors denoting the slip (twin shear) direction and the slip (twin) plane normal, respectively. The subscript *o* on $\mathbf{S}$

reminds us that these are defined using the initial crystal orientation and therefore the **S** tensors are known a priori. The superscripts α and β enumerate the available slip systems (total of N^s) and the available twin systems (total of N^{tw}), respectively. $\dot{\gamma}^\alpha$ represents the slip shear rate on a slip system α. Unlike slip, deformation twinning is characterized by a constant amount of shear and the volume fraction of the crystal experiencing deformation twinning evolves with the imposed deformation. Treating deformation twinning as a pseudo-slip mechanism, the homogenized shear rate in the crystal is described by $\dot{f}^\beta \gamma_{tw}^\beta$, where γ_{tw}^β represents the amount of constant shear associated with twin system β and f^β denotes its volume fraction in the given crystal.

Power-law relations have been employed to quantify the plastic shearing rate on slip and twin systems using the visco-plastic approach of Asaro and Needleman [17]:

$$\dot{\gamma}^\alpha = \dot{\gamma}_o \left| \frac{\tau^\alpha}{s^\alpha} \right|^{1/m} sign(\tau^\alpha), \tag{2.7}$$

$$\dot{f}^\beta = \begin{cases} \dfrac{\dot{\gamma}_o}{\gamma_{tw}^\beta} \left| \dfrac{\tau^\beta}{s^\beta} \right|^{1/m} & \text{if} \quad \tau^\beta \geq 0 \\ 0 & \text{if} \quad \tau^\beta \leq 0 \end{cases}. \tag{2.8}$$

In this study, the rate sensitivity parameter, *m*, was assumed to be the same for both slip and twinning. A very low value of *m* = 0.02 was used to simulate almost rate-independent behavior of metals at room temperature. The reference slip rate, $\dot{\gamma}_o$, was arbitrarily set as 0.001 s^{-1} to reflect the interest in quasi-static loading conditions. τ^α (τ^β) and s^α (s^β) represent the resolved shear stresses and the shear resistance for a particular slip (twin) system. Note that, unlike slip, a positive resolved shear stress is

needed for twinning. The resolved shear stress for both slip and twin systems can be defined as

$$\tau^{\alpha} \approx \mathbf{T}^{*} \bullet \mathbf{S}_{o}^{\alpha} . \qquad \textbf{(2.9)}$$

2.2.2 *Criterion for Grain Fragmentation*

In the present model, when the twin volume fraction in a given grain ($\sum_{\beta} f^{\beta}$) reaches a predetermined saturation value (f_{sat}), that grain is fragmented into parts: a parent grain (corresponding to the untwinned or matrix region) and several offspring grains (corresponding to the dominant twin systems in that grain). In this study, f_{sat} was set equal to 0.4 based on the experimental observations reported by Salem et al. [8, 13]. The volume fractions of the parent and the offspring grains are determined by the accumulated twinning activity in the grain up to the point of fragmentation. It is ensured that the sum of the volume fractions of the parent and the offspring grains is equal to one. Once the grain is fragmented, the volume fractions of the newly created grains are kept constant during the rest of the deformation. Consequently, the number of new orientations produced in this model simply equals to the number of offspring grains created in the fragmentation process. Only the twin systems with a volume fraction larger than 0.1 were represented as newly created grains in this study. The volume fractions associated with the non-dominant twin systems (defined here as $f^{\beta} < 0.1$) have been transferred to the most dominant twin system.

2.2.3 *Grains after Fragmentation*

Note that the slip activities in the offspring grains are tantamount to slip in the twinned regions of the original grain. After grain fragmentation, the newly formed grains (parent and offspring grains) are essentially treated as independent grains. Moreover, further plastic deformation in these grains is assumed to be fully accommodated by crystallographic slip alone. Note that, in the total Lagrangian framework employed in this work, the slip tensors ($\mathbf{S}_o^\alpha$ in Eq. (2.6)) in the newly created grains are defined based on the orientations of the twinned regions in the intermediate relaxed configuration. As noted earlier, the twin orientations in the intermediate configuration are known a priori, and are conveniently described by a 180 degree rotation about the twin habit plane normal for the α-Ti single crystals. The treatment of the grains before and after fragmentation is summarized in Figure 2. The following salient features of the new model presented here are worth noting:

(1.) Before fragmentation, deformation twinning is treated as a pseudo-slip mechanism. So there is only a single decomposition of the total deformation gradient tensor. Consequently, the matrix and the twinned regions have a pre-defined orientation relationship. In other words, the twin regions rotate with the matrix as if they were rigid inclusions attached to the matrix with a specific orientation relationship.

(2.) After fragmentation, the newly formed grains behave independent of the parent grain and each other. Following the Taylor approach [40], the matrix and the twins are assumed to experience the same total deformation gradient tensor. However, the plastic deformation gradient, the elastic stretch and the lattice rotation are expected to differ substantially among the parent and each of the offspring grains. Note also that the special orientation relationship between the parent and offspring grains is still

maintained in the intermediate relaxed configuration (even after grain fragmentation), but is expected not to be retained in the final configuration (because the parent and offspring grains are generally expected to experience different lattice rotations after the fragmentation event).

The response of a polycrystalline aggregate is obtained here using the extended Taylor assumption of uniform deformation gradient tensor in the entire polycrystal. Consequently, the overall Cauchy stress tensor in the polycrystal is assumed to be given by the volume averaged value of the Cauchy stress tensor in all of the constituent grains (including all of the parent and the offspring grains).

2.3. Strain Hardening Functions

Description of the evolution of the slip and twin resistances during plastic deformation has been a very difficult problem in the development of robust crystal plasticity models for hcp metals such as titanium. The slip-twin interactions are fairly complex [8, 41, 42], and there is thus far only a limited amount of quantitative experimental data available. In this study, a phenomenological description of the slip and twin hardening laws has been proposed.

2.3.1 *Strain Hardening Prior to Fragmentation*

Some of the most successful phenomenological descriptions to date have been the saturation-type hardening laws that can be generically expressed as

$$\dot{s}^{\alpha} = h_s^{\alpha}\left(1-\frac{s^{\alpha}}{s_s^{\alpha}}\right)\sum_{k}^{N^s}\dot{\gamma}^{k}\ , \qquad \textbf{(2.10)}$$

in which h_s^α and s_s^α represent the hardening rate and the saturation value associated with the slip system α, respectively. Implicit in Eq. (2.10) is the assumption of isotropic latent hardening which implies that activity on one slip system results in equal hardening of all potential slip systems. In a recent paper, Salem et al. [23] used extended versions of the saturation-type hardening functions to capture the complex interactions between slip and twinning. In that study, Eq. (2.10) has been used for slip hardening, while allowing the slip hardening rate and the saturation values to evolve with deformation twin activity as

$$h_s^\alpha = h_s(1 + C(\sum_\beta f^\beta)^b), \tag{2.11}$$

$$s_s^\alpha = s_{so} + s_{pr}(\sum_\beta f^\beta)^{0.5}. \tag{2.12}$$

The functional forms of Eqs. (2.11) and (2.12) were motivated by experimental observations in deformation studies on high-purity α-Ti. The parameters h_s and s_{so} denote the hardening rate and the saturation value, respectively, in the absence of twinning. C, s_{pr} and b are hardening parameters that aim to capture phenomenologically the complex interactions between slip and deformation twinning. $\sum_\beta f^\beta$ denotes the total twin volume fraction in the grain.

In the present work, it is essential to allow the hardening parameters in Eqs. (2.11) and (2.12) to take on different values for the different slip families (Table 1) in order to obtain better predictions of the anisotropic stress-strain responses subjected to various deformation paths. A total of 18 slip systems belonging to three distinct slip families and 12 twin systems belonging to two distinct twin families were considered. A schematic for

twin and slip systems in a single crystal of α-titanium is shown in Appendix C. Eqs. (2.10) - (2.12) were reformulated as

$$\dot{s}^{\alpha} = h_s^{pri}(1-\frac{s^{\alpha}}{s_s^{\alpha}})\sum_{k}^{N_{pri}^s}\dot{\gamma}^k + h_s^{bas}(1-\frac{s^{\alpha}}{s_s^{\alpha}})\sum_{l}^{N_{bas}^s}\dot{\gamma}^l + h_s^{pyr}(1-\frac{s^{\alpha}}{s_s^{\alpha}})\sum_{m}^{N_{pyr}^s}\dot{\gamma}^m \ , \tag{2.13}$$

$$h_s^{pri} = h_{so}^{pri}(1+C(\sum_{\beta} f^{\beta})^b)\ , \quad h_s^{bas} = h_{so}^{bas}(1+C(\sum_{\beta} f^{\beta})^b)\ , h_s^{pyr} = h_{so}^{pyr}(1+C(\sum_{\beta} f^{\beta})^b)\ , \tag{2.14}$$

$$s_s^{\alpha} = \begin{cases} s_{so}^{pri} + s_{pr}(\sum_{\beta} f_{\beta})^{0.5} & if \quad \alpha \in \text{prism slip systems} \\ s_{so}^{bas} + s_{pr}(\sum_{\beta} f_{\beta})^{0.5} & if \quad \alpha \in \text{basal slip systems} \\ s_{so}^{pyr} + s_{pr}(\sum_{\beta} f_{\beta})^{0.5} & if \quad \alpha \in \text{pyramidal slip systems} \end{cases} . \tag{2.15}$$

The experimental observations of Salem et al. [13, 43] indicate that twinning occurs profusely in a short intermediate strain range. Consequently, the twin resistances were treated as constants prior to grain fragmentation.

2.3.2 *Strain Hardening after Fragmentation*

After fragmentation, slip resistances of the various slip systems in the parent and offspring grains have been assigned the same values that were in the grain prior to fragmentation. However, the resistance for any twin system in the parent and the offspring grains is assumed to be very high to prevent further twinning. The evolution of slip resistances in subsequent deformation continues as described by Eqs. (2.13) – (2.15).

2.4. Conclusions

A new crystal plasticity model has been formulated to simulate the anisotropic stress-strain response and texture evolution for α-titanium during large plastic strains at room temperature. The major new features of the model include: (a) incorporation of slip inside twins as a significant contributor to accommodating the overall imposed plastic deformation, and (b) extension of slip and twin hardening laws to treat separately the hardening behavior of the different slip families (prismatic <a>, basal <a>, and pyramidal <c+a>) using hardening parameters that are all coupled to the extent of deformation twinning in the sample. In particular, the novel grain-fragmentation scheme was inspired by the recent experimental observations and has been demonstrated to be capable of efficiently handling the large number of new orientations created by deformation twinning. It is important to recognize that deformation twinning is treated as a pseudo slip before fragmentation and the twins are treated as independent grains after fragmentation. The proposed model will be calibrated and evaluated in the next chapter by direct comparison with the experimental measurements.

CHAPTER3: CALIBRATION AND EVALUATION

3.1. Experiments on α-Titanium

Most of the experimental measurements used in this work were provided by our collaborators: (1) Dr. Ayman A. Salem at Air Force Research Laboratory (AFRL), and (2) Dr. Carl Necker at Los Alamos National Laboratory (LANL). The basic procedures and techniques used for obtaining the required measurements are briefly introduced in this section.

3.1.1. *Material*

This investigation utilized two grades of pure α-titanium: (1) a high-purity grade (99.9998%) supplied by the Alta Group of Johnson Matthey Electronics, Inc. as a clock-rolled disk (12-mm thick), and (2) a commercial-purity titanium (grade-2) that was received as a 33-mm thick hot rolled plate. A summary of the chemical composition of both materials is provided in table 2. Both materials were given recrystalization heat treatments to produce equiaxed grain structures. The annealed high purity α-titanium had an average grain size of 30 μm while the annealed commercial purity α-titanium had an average grain size of 35 μm. The annealed textures of both materials were measured by Orientation Imaging Microscopy (OIM) technique. The annealed high purity α-titanium showed a strong fiber texture (Figure 3(a)) and its (0001) pole figures indicate that the c-axes of many grains in this sample lie about 20-35 degrees to the plate normal (labeled ND). The annealed commercial purity α-titanium had a typical rolling texture (Figure 3(b)) with the (0001) pole figures titled about 35-40 degrees from normal direction to the

rolling direction (labeled RD). Additional information about these materials is given in references [8, 13, 43].

3.1.2 *Mechanical Testing and Metallography*

The stress-strain behavior in both materials was established via isothermal compression tests conducted on cylindrical samples at a constant strain rate of 0.01 s^{-1}. The deformed samples were prepared for microscopy by a set of metallographic preparation steps including sectioning, grinding, mechanical polishing, electro-polishing and chemical etching. Additional information about mechanical testing and metallography is given in references [8, 13, 43].

3.1.3 *Measurements*

Three stress-strain measurements (two from simple compression tests and one from simple shear test) and the corresponding strain hardening plots for high-purity titanium samples were available from previous studies [23, 43]. Three stress-strain measurements (all from simple compression tests) for commercial-purity titanium samples were provided by Dr. Ayman A. Salem at AFRL. The measurements of the initial textures for both materials (Figure 3) and the measurement of deformed texture in simple shear test for high purity α-titanium were also available from the earlier work. These texture measurements were obtained by Orientation Imaging Microscopy (OIM) technique. In order to evaluate the proposed model, five new texture measurements were acquired for deformed samples in simple compression test: two for high-purity titanium and three for commercial-purity titanium. These new measurements were provided by Dr.

Carl Necker at LANL. They were obtained by X-ray diffraction (XRD) technique on a Scintag X1 5-axis pole figure goniometer using Cu-K_α radiation. The beam is a point source, circularly collimated to 0.8mm. The detector is a Peltier cooled solid-state detector with a slit of 2mm. The samples had a minimum of $1cm^2$ surface area. The $(10\bar{1}0)$, (0001), $(10\bar{1}1)$, $(10\bar{1}2)$, $(11\bar{2}0)$, and $(10\bar{1}3)$ pole figures were measured. The samples were oscillated 4 mm to collect data from as many grains as possible. Data was collected out to 80˚ sample tilt in 5˚ sample rotation and tilt increments with a two second counting time. The data was analyzed using the popLA software [44], to produce corrected and recalculated pole figures and orientation distributions. The raw data was corrected for background and defocusing using a correction file generated from a titanium sample with a random texture. The data was then run through a harmonics algorithm to extrapolate the outer fringes of the pole figure data and then the data was re-normalized. This data was run through the WIMV algorithm to produce recalculated pole figures and orientation distribution functions.

3.2. Calibration: Determination of Model Parameters

There are a total of fourteen material parameters in the crystal plasticity model presented in chapter 2 (Table 1). The goal here is to establish the values of these parameters by curve-fitting the predicted stress-strain responses in selected deformation modes to the corresponding experimental measurements. This procedure was first established for high purity α-titanium. Once the approach was validated, it was easily extended to commercial purity α-titanium. Previous studies [23] have established a similar approach for accomplishing this task. This approach recognizes the influence the

different parameters have on the form of the predicted stress-strain curves and uses repeated trials until the predictions match the measurements. In this process, the present study revealed that some of the parameters for the different slip families in Eqs. (2.13) - (2.15) exhibited similar values. Based on these observations, the following assumptions were made to reduce the number of hardening parameters from fourteen to eleven:

$$h_{so}^{pri} = h_{so}^{bas} = h_{so}^{pri-bas}, \quad s_{so}^{bas} = s_{so}^{pyr} = s_{so}^{bas-pyr}, \quad s_{tw}^{com} = s_{tw}^{ten} = s_{tw} \tag{3.1}$$

The values of all the eleven parameters were established by fitting the predicted stress-strain curves to the corresponding measurements in two different monotonic deformation modes (simple compression and simple shear). Briefly, the following steps were used to establish the hardening parameters:

(1) The values of initial resistances (s_o^{pri}, s_o^{bas} and s_o^{pyr}) on different slip families (basal <a>, prism <a>, and pyramidal <c+a>) were determined by fitting the predicted yield strengths in simple compression along ND and in simple shear to the corresponding measurements (Figure 4).

(2) The value of initial resistance (s_{tw}) for twinning was determined by matching the start of stage B in the predicted strain hardening plot in simple compression along ND (Point 2 in Figure 5) to the corresponding measurement. Recently, this point on the strain hardening plot curve has been correlated with the onset of deformation twinning [13].

(3) The values of slip hardening parameters ($h_{so}^{pri-bas}$, h_{so}^{pyr}, s_{so}^{pri} and $s_{so}^{bas-pyr}$) were determined by fitting the stage A of strain hardening plot (Figure 5) and the stress-strain curve in simple shear (Figure 4) in which the volume fraction of deformation twinning is

not significant and therefore slip is considered as the main mechanism to accommodate plastic deformation.

(4) The values of coupled slip-twin hardening parameters (b and C) were determined by fitting the stage B of strain hardening plot (Figure 5) where the increase of strain hardening rate is correlated to the increasing twin volume fraction.

(5) The value of saturation hardening parameter (s_{pr}) was determined by fitting the ND simple compression stress-strain curve (Figure 4) at large strains where it appears to approach saturation.

Using above strategy, all model parameters for high purity α-titanium were estimated and summarized in Table3. In analogous treatment, the model parameters for commercial purity α-titanium were established by fitting the predicted stress-strain curves to the measurements (Figures 6(a) and 6(b)). The values of the model parameters are shown in Table 4. The key subroutines in the numerical code developed for this calibration procedure are attached in Appendix D.

3.3. Evaluation: Comparison with Measurements

3.3.1. *Stress-strain Responses*

In this section, the proposed model and the associated hardening laws were evaluated quantitatively by directly comparing the predictions to the measurements that were not used in the calibration process. The predicted stress-strain response in simple compression along TD for high-purity titanium showed good agreement with the measurement (Figure 4). It is worth noting that the starting texture for the compression

test along TD is significantly different compared to the starting texture for compression test along ND (Figure 7). Note also that the flow stress in compression along TD is substantially lower than the flow stress in compression along ND. The predicted stress-strain response in simple shear (Figure 4) also showed good agreement with measurement up to shear strain $(\gamma) \approx 0.6$, but an overestimation of about 20% on the flow stress was observed at larger strains ($\gamma \approx 1.0$ in Figure 4). It is worth noting that at large shear strains the shear samples often develop macroscale shear bands and this could lower the measured flow stresses.

The stress-strain curves in Figure 4 were plotted as equivalent stress – equivalent strain curves. While the concept of a Mises-equivalent stress has no relevance for anisotropic plasticity, it helps us understand the degree of anisotropy exhibited by the material. If the material exhibited isotropic plastic response, all of the curves shown in Figure 4 should be identical. The spread between the stress-strain responses in the different deformation modes (about a factor of 2 between simple compression and simple shear) provided us a measure of the degree of anisotropy exhibited by the high purity α-Ti that is largely attributable to the underlying crystallographic texture in the sample. This degree of anisotropy appears to be well captured by the Taylor-type crystal plasticity model presented in the current work.

The stress-strain curve in simple compression along RD for commercial-purity titanium was not used in the calibration procedure and therefore it can be utilized for evaluation. The predicted stress-strain response showed good agreement with measurement (Figure 6(c)).

3.3.2. *Texture Evolution*

The texture measurements are not utilized for calibration and hence they can be used for evaluation. Texture predictions for simple compression along ND in high-purity titanium at two strains ($\varepsilon = -0.22$ and $\varepsilon = -1.00$) showed good agreement with the measurements (Figures 8 and 9). At $\varepsilon = -0.22$, both the prediction and the measurement exhibited two major c-axis fiber texture components (easily seen in (0001) pole figure). The first fiber has its c-axis about 15-30° from ND, while the second fiber has its c-axis about 75-90° from ND. The first component was associated with the matrix, and the second component with the twins, in a prior study [8]. A similar texture was observed in (0001) pole figure at $\varepsilon = -1.00$, where the intensity of the component associated with twinning increased substantially (Figure 9).

Texture predictions for simple shear at $\gamma = -1.00$ in high-purity titanium showed reasonable agreement with the corresponding measurement (Figure 10), especially in the $(10\bar{1}0)$ pole figure where six strong texture components are clearly seen. The predicted (0001) pole figure captured the strong texture component located about 20-40° from ND. However, the predicted (0001) pole figures missed the weaker texture components located around the rim (Figure 10).

Texture predictions for simple compression tests along ND, RD and TD in commercial-purity titanium showed good agreement with corresponding measurements (Figure 11). At $\varepsilon = -1.00$, both the predictions and the measurements exhibited two major c-axis fiber texture components: one is about 10-30° from ND and the other is about 80-90° from ND. It is important to note that these compression tests yielded very similar deformed textures (at $\varepsilon = -1.00$) although their starting textures are significantly

different (Figure 12). This observation could be attributed to the fact that different twin families (compressive or tensile twins) dominate the texture evolution in different compression tests. A further investigation on the roles of different twins in these tests, especially at relatively small strains ($\varepsilon \leq -0.2$), is required to justify the above hypothesis.

3.4. Discussion: Effects of Taylor Assumption

The crystal plasticity model presented here is built on the Taylor assumption of uniform deformation gradient in all of the constituent grains. It should be intuitively expected that this gross simplification should have a strong effect on the predictions. It is well known from prior studies in this field that the Taylor assumption leads to significantly stronger textures than the experimentally measured ones [45-47]. It should also be expected that the error in the Taylor assumption would be higher for the hcp metals studied here compared to the more plastically isotropic cubic metals studied in previous work [15, 30, 37]. It is a feeling that many of the discrepancies reported here between the measurements and the predictions are attributable to the Taylor assumption employed in this study.

Although the stronger effects of Taylor assumption on hcp metals are usually alleged to be the consequence of higher plastic anisotropy in the grain, the quantitative evaluation of the influence of plastic anisotropy is not available yet in literature for hcp materials. This might be mainly caused by the fact that the experimental data for characterizing the plastic parameters at the crystal level is very limited and even conflicting for this class of materials. In the current study, the plastic parameters (critical

resolved shear stresses of slip and twin systems) established from the crystal plasticity model were selected as the variables for evaluating the effects of plastic anisotropy. Stress and strain distributions over a deformed polycrystalline material were selected to reflect the effects of Taylor assumption. The distributions obtained from finite element simulation are considered as "accurate" results because finite element models satisfy both compatibility and equilibrium throughout the polycrystal.

This comparison was conducted at small strain (2% reduction) in plane strain compression (since the differences between Taylor predictions and FE predictions are most significant in this mode of deformation [46]). Deformation twinning was not considered in this analysis due to the following two reasons: (1) the volume fraction of twinning at this strain level is very small [8, 13] and hence it is ignorable, and (2) the finite element model including deformation twinning is not available at this point. Consequently, the plastic anisotropy of an hcp crystal is solely decided by the ratio of critical resolved shear stresses in the three slip families (basal <*a*>, prism <*a*> and pyramidal <*c*+*a*>). In this work, the evaluation was performed at three different levels of plastic anisotropy: (1) 1-1-1, (2) 5-1-4, and (3) 15-1-10. In order to understand the major differences between the FE simulations and the simulations with the Taylor assumption, the statistics of the variation in the components of the local deformation gradient tensor (F_{33}) and the local Cauchy stress tensor (σ_{33}) have been investigated. Recall that the Taylor assumption imposes the same deformation gradients throughout the polycrystal and hence violates the equilibrium between grains. Therefore, the selected local variables (F_{33} and σ_{33}) should be able to reflect the strong differences between FE and Taylor-type simulations.

The material used in this work is 4,096 high-purity titanium crystals with random texture. In the finite element mesh, a total of 8,000 (20x20x20) elements were used for this simulation and only the internal 4,096 (16x16x16) elements were selected for analysis. This treatment was used to reduce the chances that final results are somewhat influenced by the imposed boundary conditions. Furthermore, for each level of plasticity anisotropy, the finite element simulation was repeated several times (in this study the simulation was executed five times and assumed that it was enough) and the data for the analysis were the averaged values from these simulations. Before each simulation, the 4,096 crystal orientations were re-shuffled and then randomly assigned to 4,096 elements. This strategy is used to ensure that the neighboring elements of any element in the FE mesh have initially random texture.

The stress and strain distributions obtained for 4,096 random orientations from Taylor-type model and finite element simulation were extracted and plotted in figure 13. It is clearly observed that both strain and stress distributions between these two models become more and more divergent as the plastic anisotropy ratio is increased from 1-1-1 to 5-1-4 to 15-1-10. Particularly, the peak values of percentage of grains obtained from Taylor-type model at ratio 15-1-10 are significantly higher than the values from finite element method. On the other hand, the distributions are much wider in finite element simulation. It is important to recognize that the plastic anisotropy ratio 5-1-4 is the actual ratio that was used for the critical resolved shear stresses in the proposed Taylor-type crystal plasticity model. At this level of plastic anisotropy ratio, the discrepancy of stress and strain distributions between Taylor model and finite element method is obvious,

which indicates that a better averaging method than Taylor assumption has potential to significantly improve the model predictions shown in section 3.3.

The focus of the current study is to incorporate new deformation mechanism (slip inside twinning) and develop better slip-twin hardening functions at single crystal level, which is independent of the choice of averaging schemes. However, realizing the considerable improvement of the prediction one can achieve by using a better averaging method, the current effort is to implement the crystal plasticity model described here in a finite element framework which averts the need for the simplifying Taylor assumption.

3.5. Conclusions

The proposed Taylor-type crystal plasticity model for predicting texture evolution and anisotropic stress-strain behavior in α-titanium has been calibrated and evaluated in this chapter. Reasonable agreement between model predictions and experimental measurements has been observed for both the anisotropic stress-strain responses and the evolved deformation textures in two different chemical compositions of α-titanium along different monotonic deformation paths: (a) high purity α-titanium: simple compression along ND, simple compression along TD and simple shear in the RD-TD plane; (b) commercial purity α-titanium: simple compression along ND, RD and TD, respectively.

To the best of our knowledge, it is the first time in the literature that crystallographic slip, deformation twinning and slip inside twinning were all incorporated into a crystal plasticity model which was evaluated for both the anisotropic stress-strain response and texture evolution in multiple deformation paths on a given hcp metal.

Moreover, this new framework has been successfully applied to two different compositions of α-titanium (two different purity levels).

CHAPTER4: ELASTIC-PLASTIC PROPERTY CLOSURES FOR HEXAGONAL CLOSE-PACKED POLYCRYSTALLINE METALS USING FIRST-ORDER BOUNDING THEORIES

4.1. Introduction

Property closures delineate the complete set of theoretically feasible macroscale (homogenized) anisotropic property combinations in a given material system, and are very useful in optimizing the performance of engineering components. In recent papers, novel mathematical procedures have been presented to successfully delineate elastic-plastic property closures based on elementary (first-order) bounding theories [48-50] as well as sophisticated higher-order homogenization theories [51-57]. This framework has been called Microstructure Sensitive Design (MSD) [24, 26], and is rigorously grounded in the efficient spectral representation of invertible linkages between the statistical description of the relevant details of the microstructure and its effective properties.

A central feature of MSD is the construction of a compact and convex microstructure hull in Fourier space that encompasses the complete set of theoretically feasible statistical distributions that quantitatively describe the relevant details of the microstructure at different levels of desired statistics (typically classified as *n*-point statistics [55, 58-60]). When the microstructure variable of interest is the crystallographic texture (corresponds to 1-point statistics of lattice orientation; also referred to as the Orientation Distribution Function or ODF), the microstructure hull is simply referred to as the texture hull. Note that each element of the texture hull corresponds to a distinct texture or ODF. Corresponding to each element of the texture hull, it is then possible to visualize a region of theoretically feasible property combinations based on the elementary

bounding theories. The union of all such feasible property combinations corresponding to all elements of the texture hull is simply the property closure [27].

In practice, brute-force identification of the property closure by a rigorous consideration of each and every element of the texture hull is highly inefficient because of the large number of dimensions of the Fourier space involved. For example, in prior work on cubic-orthorhombic textures[1], Kalidindi et al. found that it was necessary to explore twelve dimensions of the Fourier space to get sufficient accuracy in the prediction of the plastic yield properties [26]. Therefore, even with a modest discretization of the texture hull into 10 units in each dimension, the brute-force approach would require a consideration of 10^{12} distinct textures to identify the property closure. A number of computational methodologies were formulated in recent years [24, 25, 28] to overcome this difficulty. These methodologies have focused mainly on the boundary of the property closure, and sought to identify these boundary points as solutions to appropriately formulated optimization problems. In recent papers [28, 61], several closures for cubic-orthorhombic textures were successfully presented using optimization techniques such as sequential quadratic programming and Pareto-front methods [62]. In fact, it was also observed that for several property closures of interest in cubic-orthorhombic textures, the boundary points of the property closure correspond to the same set of textures for all cubic metals with a given family of slip systems [63].

Extension of the methods described above to the lower symmetry, and more plastically anisotropic, hcp metals is significantly hampered by the fact that the relevant number of dimensions in the Fourier space is considerably higher. For example, in the

[1] The first symmetry in this notation refers to symmetry at the crystal level (resulting from the atomic arrangements in the crystal lattice) while the second refers to symmetry at the sample scale (resulting from processing history); this notation is widely used by the texture community.

present study, it was found to be necessary to explore 57 dimensions of the Fourier space in order to obtain reasonably accurate results for hexagonal-orthorhombic textures of interest in high purity α-Ti. At this level of complexity, several of the optimization methods described in the earlier papers [26, 28] that worked well for cubic metals, did not perform as well for the hexagonal metals.

A new computational approach has been successfully formulated to delineate several elastic-plastic property closures of interest for hexagonal polycrystals. This new approach is introduced in this thesis and demonstrated with examples. I start by first developing an MSD framework for hcp polycrystals and then describe the new computational procedures for delineation of elastic-plastic closures for this class of materials. To the best of my knowledge, this is the first report of the application of the MSD framework to hcp polycrystals, and the first depiction of elastic-plastic closures in this important class of material systems.

4.2. Application of MSD framework to HCP Polycrystals

4.2.1. *Texture Hull*

As stated earlier, the main interest in this study is limited to 1-point statistics of lattice orientation in the hcp polycrystals with orthorhombic sample symmetry. The local state space describing the set of distinct orientations relevant to a selected class of textures is referred to as the fundamental zone (FZ) [36]. For hexagonal-orthorhombic textures, the fundamental zone is expressed in the Euler space (using Bunge-Euler angles φ_1, Φ, φ_2 [36]) as

$$\mathrm{FZ} = \left\{ g = (\varphi_1, \Phi, \varphi_2) \middle| 0 \le \varphi_1 \le \frac{\pi}{2}, 0 \le \Phi \le \frac{\pi}{2}, 0 \le \varphi_2 \le \frac{\pi}{3} \right\}. \quad \textbf{(4.1)}$$

The ODF, denoted as $f(g)$, reflects the normalized probability density associated with the occurrence of the crystallographic orientation g in the sample,

$$\frac{dV_g}{V} = f(g)dg\,, \qquad \int_{FZ} f(g)dg = 1.0\,, \quad \textbf{(4.2)}$$

where V denotes the total sample volume and dV_g is the sum of all sub-volume elements in the sample that are associated with a lattice orientation that lies within an incremental invariant measure, dg, of the orientation of interest, g. Hexagonal-orthorhombic ODFs can be expressed in a Fourier series using generalized spherical harmonic (GSH) functions [36] as

$$f(g) = \sum_{\ell=0}^{\infty} \sum_{\mu=1}^{\mathrm{M}(\ell)} \sum_{\nu=1}^{\mathrm{N}(\ell)} F_\ell^{\mu\nu}\, \ddot{T}_\ell^{\mu\nu}(g), \quad \textbf{(4.3)}$$

where $\ddot{T}_\ell^{\mu\nu}$ denote the symmetrized GSH functions and $F_\ell^{\mu\nu}$ represent uniquely the ODF. Note also that Eq. (4.3) allows the visualization of ODF as a single point in an infinite dimensional Fourier space (coordinates given by $F_\ell^{\mu\nu}$). The set of all such points, corresponding to the complete set of all physically realizable[2] ODFs, is called the texture hull in the MSD framework [25, 26]. Visualization of these infinite dimensional texture hulls poses serious challenges. The first five non-zero Fourier coefficients in Eq. (4.3) are F_2^{11}, F_2^{12}, F_4^{11}, F_4^{12} and F_4^{13}. If one wants to plot the projections of the texture hulls in three-dimensional sub-spaces, a total of ten different plots are needed to show all

[2] The term physically realizable texture is used here to refer to a texture that can be physically described or imagined. It is anticipated that a large number of these are not yet achievable in practice by currently known manufacturing options.

distinct projections for the first five dimensions of the texture hull. These plots are shown in Figure 14, and to the best of our knowledge this is the first time the hcp-orthorhombic texture hulls have been plotted and reported in literature. It should be recognized that any physically realizable texture has to have a representation inside *all* of the depicted hulls in Figure 14. Note also that the texture hulls are compact and convex in any of their subspaces [24].

4.2.2. *First-order Bounding Theories*

In the MSD framework, the microstructure description is then linked to its effective elastic-plastic properties using generalized composite theories. The ODF described above constitutes a first-order description of the microstructure (also referred to as 1-point statistics). Using this microstructure description, only the bounds of the effective elastic and plastic properties can be evaluated. Higher order descriptions, called *n*-point spatial correlation function, are also possible to obtain better estimates of the macroscale effective properties [55, 58-60]. For hexagonal-orthorhombic textures, the elementary bounds on effective elastic stiffness parameters, C^*_{ijkl}, can be expressed as (no implicit summation on repeated indices in the following set of equations[3]) [28, 48-50]

$$\left(\overline{S}^{-1}\right)_{ijij} \leq C^*_{ijij} \leq \overline{C}_{ijij}, \tag{4.4}$$

$$\max\left(\overline{C}_{iijj}, \left(\overline{S}^{-1}\right)_{iijj}\right) - \sqrt{\Delta_i \Delta_j} \leq C^*_{iijj} \leq \min\left(\overline{C}_{iijj}, \left(\overline{S}^{-1}\right)_{iijj}\right) + \sqrt{\Delta_i \Delta_j}, \quad when \ \ i \neq j, \tag{4.5}$$

$$with \quad \Delta_i = \overline{C}_{iiii} - \left(\overline{S}^{-1}\right)_{iiii}. \tag{4.6}$$

[3]The Einstein convention of implicit summation on repeated indices is employed in this work, except when explicitly noted otherwise.

In Eqs. (4.4)-(4.6), the bars on top of a field quantity denote its volume averaged value, and **C** are **S** are the local fourth-rank elastic stiffness and elastic compliance tensors, respectively.

The effective plastic yield properties are bounded rigorously on the upper side by the Taylor-type model [40], and approximately on the lower side by the Sachs model [64]. As an example, in evaluating σ_{y1} using the Taylor-type model, the following macroscopic isochoric velocity gradient is imposed on each crystal:

$$\overline{L}_{ij} = L_{ij} = \begin{pmatrix} \dot{\bar{\varepsilon}} & 0 & 0 \\ 0 & -q\dot{\bar{\varepsilon}} & 0 \\ 0 & 0 & -(1-q)\dot{\bar{\varepsilon}} \end{pmatrix}, \tag{4.7}$$

where q can take any value between 0 and 1. The local stresses, $\sigma'_{ij}(q)$, computed by the Taylor model are purely deviatoric. The hydrostatic component is computed by establishing the value of q (denoted as q^*) for which the averaged lateral stresses over the polycrystal are equal to each other, i.e. $\overline{\sigma}'_{33}(q^*) = \overline{\sigma}'_{22}(q^*)$. The yield strength of the polycrystal in the $\mathbf{e}_1$-direction is then computed as

$$\sigma_{y1} = \overline{\sigma}'_{11}(q^*) - \overline{\sigma}'_{22}(q^*). \tag{4.8}$$

The R-ratio represents the ratio of the true width strain to the true thickness strain in a tensile test and is an example of an effective plastic property of the metal that is typically of interest in metal shaping operations. The R_1 value (corresponding to tensile loading in the $\mathbf{e}_1$-axis) can then be defined as

$$R_1 = \frac{q^*}{1-q^*}. \tag{4.9}$$

4.2.3. *Spectral Representation*

The first-order microstructure-property linkages described above can be transformed into Fourier space. The components of the elastic stiffness tensor for an hcp crystal can be expressed in a crystal reference frame using five fundamental elastic constants C_{11}, C_{12}, C_{13}, C_{33} and C_{44} as

$$\begin{aligned} C^{c}_{ijkl} &= C_{12}\,\delta_{ij}\delta_{kl} + C_{44}\left(\delta_{ik}\delta_{jl} + \delta_{il}\delta_{kj}\right) + \left(C_{13} - C_{12}\right)\sum_{t=1}^{2}\left(\delta_{it}\delta_{jt}\delta_{k3}\delta_{l3} + \delta_{i3}\delta_{j3}\delta_{kt}\delta_{lt}\right) \\ &+ \left(C_{33} - C_{11}\right)\delta_{i3}\delta_{j3}\delta_{k3}\delta_{l3} + \left(C_{11} - C_{12} - 2C_{44}\right) \\ &\left(\sum_{t=1}^{3}\delta_{it}\delta_{jt}\delta_{kt}\delta_{lt} + \frac{1}{2}\left(\delta_{i1}\delta_{j2}\delta_{k1}\delta_{l2} + \delta_{i1}\delta_{j2}\delta_{k2}\delta_{l1} + \delta_{i2}\delta_{j1}\delta_{k1}\delta_{l2} + \delta_{i2}\delta_{j1}\delta_{k2}\delta_{l1}\right)\right), \end{aligned} \tag{4.10}$$

where δ_{ab} represents the Kronecker function. The components of the same tensor in the sample reference frame are expressed using the coordinate transformation law for fourth-rank tensors as

$$C^{s}_{ijkl} = g_{ia}\,g_{jb}\,g_{kc}\,g_{ld}\,C^{c}_{abcd}\,. \tag{4.11}$$

Substitution of Eq. (4.10) into Eq. (4.11) yields

$$\begin{aligned} C^{S}_{ijkl}(g) &= C_{12}\,\delta_{ij}\delta_{kl} + C_{44}\left(\delta_{ik}\delta_{jl} + \delta_{il}\delta_{kj}\right) + \left(C_{11} - C_{12} - 2C_{44}\right)A_{ijkl}(g) \\ &+ \left(C_{13} - C_{12}\right)B_{ijkl}(g) + \left(C_{33} - C_{11}\right)D_{ijkl}(g), \end{aligned} \tag{4.12}$$

with

$$\begin{aligned} A_{ijkl}(g) = \sum_{t=1}^{3} g_{it}g_{jt}g_{kt}g_{lt} + \\ \frac{1}{2}\left(g_{i1}g_{j2}g_{k1}g_{l2} + g_{i1}g_{j2}g_{k2}g_{l1} + g_{i2}g_{j1}g_{k1}g_{l2} + g_{i2}g_{j1}g_{k2}g_{l1}\right), \end{aligned} \tag{4.13}$$

$$\mathrm{B}_{\mathrm{ijkl}}(g)=\sum_{\mathrm{t}=1}^{2}\left(g_{\mathrm{it}}g_{\mathrm{jt}}g_{\mathrm{k3}}g_{\mathrm{l3}}+g_{\mathrm{i3}}g_{\mathrm{j3}}g_{\mathrm{kt}}g_{\mathrm{lt}}\right), \tag{4.14}$$

$$\mathrm{D}_{\mathrm{ijkl}}(g)=g_{\mathrm{i3}}g_{\mathrm{j3}}g_{\mathrm{k3}}g_{\mathrm{l3}}\ . \tag{4.15}$$

The $A_{ijkl}(g)$, $B_{ijkl}(g)$ and $D_{ijkl}(g)$ functions can be represented in a Fourier series using GSH functions. As an example, $\mathrm{D}_{\mathrm{ijkl}}(g)$ in Eq. (4.15) can be expressed in Fourier space as

$$\mathrm{D}_{\mathrm{ijkl}}(g)=\sum_{\ell=0}^{4}\sum_{\mu=1}^{M(\ell)}\sum_{\nu=1}^{N(\ell)}{}_{ijkl}\,\mathrm{D}_{\ell}^{\mu\nu}\ddot{\mathrm{T}}_{\ell}^{\mu\nu}(g). \tag{4.16}$$

The Fourier coefficients in Eq. (4.16) are computed using the standard methods of Fourier analyses as

$${}_{ijkl}\mathrm{D}_{\ell}^{\mu\nu}=(2l+1)\oint\mathrm{D}_{ijkl}(\mathrm{g})\ddot{\mathrm{T}}_{\ell}^{\mu\nu}(g)dg\ . \tag{4.17}$$

The integral in Eq. (4.17) can be evaluated numerically using Simpson method [65].

As an example, the Fourier coefficients for two diagonal elastic stiffness components, C_{1111} and $C_{1313,}$ are presented in Table 5. Note that these terms are valid for all hcp crystals. Note also the ${}_{ijkl}A_{\ell}^{\mu\nu}$, ${}_{ijkl}B_{\ell}^{\mu\nu}$ and ${}_{ijkl}D_{\ell}^{\mu\nu}$ coefficients are zero for $\ell>4$. The spectral representations in Eqs. (4.10) – (4.17) permit the easy computation of the bounds for any given hexagonal-orthorhombic texture. For example, the upper bound for the diagonal components of the macroscale elastic stiffness tensor can be expressed as (no implicit summation on repeated indices)

$$\mathrm{C}_{\mathrm{ijij}}^{*}\le\left\langle\mathrm{C}_{\mathrm{ijij}}\right\rangle=\oint\mathrm{C}_{\mathrm{ijij}}(\mathrm{g})\,\mathrm{f}(\mathrm{g})\,\mathrm{dg}=\mathrm{C}_{12}\delta_{\mathrm{ij}}+\mathrm{C}_{44}(1+\delta_{\mathrm{ij}})+\sum_{\ell=0}^{4}\sum_{\mu=1}^{\mathrm{M}(\ell)}\sum_{\nu=1}^{\mathrm{N}(\ell)}\frac{\mathrm{F}_{\ell}^{\mu\nu}}{(2l+1)}\cdot \tag{4.18}$$
$$[(\mathrm{C}_{11}-\mathrm{C}_{12}-2\mathrm{C}_{44})\,{}_{ijij}A_{\ell}^{\mu\nu}+(\mathrm{C}_{13}-\mathrm{C}_{12})\,{}_{ijij}B_{\ell}^{\mu\nu}+(\mathrm{C}_{33}-\mathrm{C}_{11})\,{}_{ijij}D_{\ell}^{\mu\nu}]$$

It is important to keep in mind that some of the bounds described earlier are functions of volume averaged quantities and not directly equal to a volume average quantity.

The macroscale yield properties from the upper bound theory are computed by imposing velocity gradient tensor in Eq. (4.7). The local crystal stresses calculated by the Taylor-type model are expressed in a Fourier series. For example, the stresses in individual crystals corresponding to the velocity gradient tensor in Eq. (4.7) can be expressed as (no implicit summation on repeated indices)

$$\sigma_{ii}^{'}(g,q)=\sum_{\ell=0}^{\infty}\sum_{\mu=\ell}^{M(\ell)}\sum_{\nu=\ell}^{N(\ell)}{}^{ii}_{y1}S_{\ell}^{\mu\nu}(q)\ddot{T}_{\ell}^{\mu\nu}(g)\,, \tag{4.19}$$

The average stress in the polycrystal is given as (no implicit summation on repeated indices)

$$\overline{\sigma}_{ii}^{'}=\sum_{\ell=0}^{\infty}\sum_{u=\ell}^{M(\ell)}\sum_{v=\ell}^{N(\ell)}\frac{{}^{ii}_{y1}S_{\ell}^{\mu\nu}(q)F_{\ell}^{\mu\nu}}{2l+1}\,. \tag{4.20}$$

The values of the Fourier coefficients ${}^{ii}_{y1}S_{\ell}^{\mu\nu}(q)$ were established again using standard methods of Fourier analyses (using an expression similar to Eq. (4.17)) and using the results from a Taylor-type crystal plasticity model calibrated to the experimental data on annealed high-purity α-Ti with an average grain size of 30 μm [66] (see Table 3). ${}^{ii}_{y1}S_{\ell}^{\mu\nu}(q)$ were computed for discrete values of q, in increments of 0.1 in the range 0.0 to 1.0, and linearly interpolated for values in between. All the Fourier coefficients needed for this computation were listed in Appendix E. The value of q (denoted as q*) for which the volume-averaged lateral stresses over the polycrystal are equal to each other is then solved from $\overline{\sigma}_{33}^{'}\left(q^{*}\right)=\overline{\sigma}_{22}^{'}\left(q^{*}\right)$. Once the value of q* is determined, Eq. (4.8) is used to derive the polycrystalline tensile yield stress for upper bound. In this work, the values of

${}^{ii}_{y1}S^{\mu\nu}_{\ell}(q)$ were established and utilized to ℓ =12. At this level of truncation, the error between the spectral representation (due to truncation of the series) and the Taylor-type model predictions for a broad set of single crystals was found to be less than 3%. Note also that the total number of Fourier dimensions for ℓ =12 in hexagonal-orthorhombic textures is 57. In other words, 57 Fourier coefficients were established for each stress component for each value of q. In prior work, the comparable accuracy in cubic polycrystals was obtained by using only the first twelve terms of the Fourier series corresponding to ℓ =8. The increased need for higher dimensions in hcp crystals is attributed both to their lower crystal symmetry as well as the inherently stronger anisotropy in their plastic properties, when compared to the cubic polycrystals.

A similar approach has also been employed to cast the Sachs' model in the Fourier space. Further details of this can be found in a recent paper on the application of the MSD framework for obtaining closures in cubic-orthorhombic textures [28].

4.3. Elastic-Plastic Property Closures

4.3.1. *Introduction*

The spectral representations described above facilitate delineation of the first-order property closures. As an example, the mathematical formulations for identifying the $\left(C^*_{1111}, C^*_{1313}\right)$ closure are presented below. Let $\widetilde{C}^*_{1313}$ denote a specific value of C^*_{1313} that lies in between its theoretical maximum and minimum values. The complete set of Fourier coefficients, $\widetilde{M}$, that can be associated with the selected value of $\widetilde{C}^*_{1313}$ can be expressed as

$$\widetilde{M} = \left\{ F_\ell^{\mu\nu} \middle| F_\ell^{\mu\nu} \in Hull, \quad \widetilde{C}^*_{1313} = \alpha \overline{C}_{1313} + (1-\alpha)\overline{S}^{-1}_{1313}, \alpha \in [0,1] \right\}, \tag{4.21}$$

where *Hull* denotes the set of all Fourier coefficients that lie on or inside the texture hull (Figure 14). Note that the values of $F_\ell^{\mu\nu}$ influence the values of $\overline{C}_{1313}$ and $\overline{S}_{1313}$ (see Eq. (4.18)). $\overline{S}^{-1}_{1313}$ in Eq. (4.21) denotes the (1,3,1,3) component of the inverse of the averaged fourth-rank compliance tensor. The maximum and minimum values of C^*_{1111} are then established as

$$\left(\widetilde{C}^*_{1111}\right)_{\max} = Max\left\{ \overline{C}_{1111} \middle| F_\ell^{\mu\nu} \in \widetilde{M} \right\} \tag{4.22}$$

$$\left(\widetilde{C}^*_{1111}\right)_{\min} = Min\left\{ \left(\overline{S}^{-1}\right)_{1111} \middle| F_\ell^{\mu\nu} \in \widetilde{M} \right\} \tag{4.23}$$

$\left(\left(\widetilde{C}^*_{1111}\right)_{\max}, \widetilde{C}^*_{1313}\right)$ and $\left(\left(\widetilde{C}^*_{1111}\right)_{\min}, \widetilde{C}^*_{1313}\right)$ constitute two of the points on the first-order closure. By letting $\widetilde{C}^*_{1313}$ vary systematically between its theoretical maximum and minimum values, the complete first-order property closure can be delineated. It should be clear from the above description that the mathematical procedures used in delineating the first-order closures are quite complex and require substantial computational effort and resources; determination of each point on the closure typically takes a few hours on a regular desktop PC.

4.3.2. *Comprehensive Property Closures for Polycrystals*

As mentioned earlier, although the above procedure for delineating elastic-plastic property closures worked well for cubic-orthorhombic textures, it did not work as well for hexagonal-orthorhombic textures. This is attributed to the fact that the plastic properties in hcp polycrystals are optimized in 57 Fourier dimensions (compared to 12

dimensions in cubic polycrystals). In this work, a novel scheme has been established to delineate the property closures for hexagonal-orthorhombic textures.

The procedure for delineating the property closures starts with a consideration of a set of points in the texture hull that correspond to "eigen textures". Because of the orthorhombic sample symmetry used in this study, each eigen texture corresponds to the texture produced by a set of four equi-volume single crystals that are selected to satisfy the orthorhombic symmetry at the sample scale. The set of eigen textures is selected while ensuring that the fundamental zone described in Eq. (4.1) is adequately covered. The property combinations for these eigen textures are first evaluated using the spectral linkages described in the previous section. Figure 15(a) shows an example of a closure for the feasible combinations of σ_{y1} and C_{1111} using the lower bound theory, based solely on the consideration of the eigen textures. A finite number of textures corresponding to the boundary of this closure (in this work twenty textures were used) were selected. The macroscale property combinations for the weighted combinations of these textures, taking one pair of textures at a time, were evaluated systematically (considering all possible combinations of pairs of the selected textures). As expected, these computations revealed that some of the property combinations outside the eigen-texture closure were indeed possible, i.e. the results expanded the closure. Once again a new set of textures corresponding to the new boundary of the expanded closure were selected (this time these were a mixture of eigen textures and non-eigen textures) and the property combinations corresponding to the weighted combinations of these (for all possible pairs of selected textures) were evaluated to see if they expanded the closure. This process was repeated until the closure did not expand in any discernable way. Figure 15(b) shows such an

expanded lower bound closure for σ_{y1} and C_{1111}. Compared to the eigen-texture closure shown in Figure 15(a), the lower bound closure in Figure 15(b) is considerably larger and more convex. The method described above to produce a closure essentially follows the main ideas underlying genetic algorithms, where good solutions are pre-selected (this was done here by selecting the textures producing property combinations on the boundary of the closure) and "mutations" or "cross-overs" (weighted combinations of textures in this approach) are explored.

In a very similar manner, the closure based on the upper bound theory is identified. For the present example, the upper bound closure is shown in Figure 15(c) along with the lower bound closure. Note that there is only a small overlap of these closures, indicating that the complete closure would indeed be significantly larger than either of the closures in Figure 15(c) based on bounding theories.

In order to determine the complete closure, it is important to recognize that all property combinations between the bounds are feasible (based on the first-order theories). Once again, a set of textures corresponding to the property combinations on the boundaries of the upper and lower bound closures were selected (in this work twenty textures were selected from each bound). For weighted combinations of the selected textures (one pair at a time as was described earlier), the set of feasible combinations of the effective properties of interest, (P^*, Q^*), were computed as

$$\left(P^* = \alpha P^{UB} + (1-\alpha)P^{LB},\ Q^* = \beta Q^{UB} + (1-\beta)Q^{LB}\right), \qquad \textbf{(4.24)}$$

where P^{UB}, Q^{UB}, P^{LB} and Q^{LB} denote the upper and lower bounds for the selected texture, and α and β were individually varied from 0.0 to 1.0. As before, the closure was expanded by repeating this basic approach, until it stopped expanding. The

corresponding complete closure for the present example is shown in Figure 15(d). Note that this closure includes all feasible property combinations as predicted by the elementary bounding theories (i.e. both upper and lower bound theories).

4.3.3. *Property Closures for Cold-Wrought Materials*

In identifying the closures shown in Figure 15, I used the values of the initial slip resistances that have been established in a recent study on annealed high purity α-Ti with an initial average grain size of 30 μm. Therefore the property combinations depicted in Figure 15(d) correspond to all possible hexagonal-orthorhombic textures in this material system (i.e. for annealed high purity α-Ti with a grain size of about 30 μm). However, it is well established that cold work dramatically alters the slip resistances in α-Ti [8, 13, 23, 66]. In order to understand the influence of hardening on the closure shown in Figure 15(d), the mathematical procedure described above was repeated for building closures using the saturated values of the slip resistance in high purity α-Ti (established in the prior work [66] and summarized in Table 3). Note that this corresponds to the material being in a heavily cold-worked condition. It is seen that the closure for the heavily cold-worked high purity α-Ti is significantly larger than the closure for the annealed high purity α-Ti (Figure 16). The corresponding property closures for commercial purity α-Ti are shown in Figure 17. Comparison of the closures in Figures 16 and 17 reveals that the purity level has a substantial influence on the both the shape and size of the identified closures. The main consequences of cold-work and the purity levels are manifested into the closures described here through the values of slip resistances. Since a much broader range of slip resistances (and their ratios) are possible in the hcp crystals, the shapes and

sizes of the closures can change much more dramatically compared to those reported earlier in cubic polycrystals [28].

The methods described above can, in principle, be applied to all hcp polycrystals. However, the required data on the slip resistances is readily available only for a limited number of material systems. Since the data for elastic stiffness is much more readily available, several examples of elastic property closures for selected hexagonal materials are demonstrated in Figure 18. A further nice feature of the elastic property closures is that their Fourier representations are exact (see Eq. (4.16)), unlike those for plastic properties that have been truncated (in this work to ℓ =12). It is seen from Figure 18 that strongly elastically anisotropic materials such as Zn and Ca exhibit significantly larger closures compared to the others.

4.3.4. *R Closures*

A particular plastic property of tremendous interest to the metal sheet working community is the R ratio (defined in Eq. (4.9)). Here, as a final example, the (R_1-σ_{y1}) closure is delineated. It has been decided to explore this closure using only the upper bound theory (i.e. a Taylor-type model) that is used extensively by researchers in this field. Since the value of q^* can range from 0.0 to 1.0, the corresponding value of R_1 can range from zero to infinity. This broad range poses significant numerical challenges. Therefore, this closure was approached in two steps: (i) delineation of (q^*-σ_{y1}) closure, and (ii) transformation of (q^*-σ_{y1}) closure into the (R_1-σ_{y1}) closure. Figure 19 shows a (q^*-σ_{y1}) closure for annealed α-Ti obtained using the procedures described earlier. An

interesting feature of the (q^* - σ_{y1}) closure is its symmetry about $q^* = 0.5$. Upon further reflection, it should be possible to convince that for every value of $q^* > 0.5$, there should be another point at (1 - q^*) at the same value of σ_{y1}; the later simply corresponds to a texture rotated by 90 degrees about the $\mathbf{e}_1$-axis. This has been verified for selected points on the closure (see textures corresponding to A, B, C and D in Fig. 19).

Figure 20 shows the (R_1- σ_{y1}) closure obtained by transforming the (q^* - σ_{y1}) closure shown in Fig. 19 using Eq. (4.9). As expected, the value of R_1 can range from zero to infinity. In Fig. 20, the closure was truncated at R_1=10. Points A, E, and D in Fig. 6 transformed to Points A', E', and D', respectively, in Fig. 20. In other words, the textures corresponding to the pairs of Points (A, A'), (D, D'), and (E, E') are exactly the same. It should be of interest to metal sheet working community to note that there exist a fairly large number of textures that can yield low values of yield strength with high values of R ratios.

4.4. Conclusions

The following conclusions are drawn from this study:

(i) It is possible to extend the MSD framework to hcp polycrystals. This means that textures in hexagonal polycrystals can also be represented in texture hulls, as was done earlier for cubic polycrystals. Examples of hexagonal-orthorhombic texture hulls were depicted in this thesis.

(ii) The lower symmetry, and the inherently higher anisotropy of plastic response, in hcp crystals results in the need for a much larger number of dimensions in the spectral framework of MSD. For example, the plastic properties associated

with cubic-orthorhombic textures were well represented in twelve dimensions (ℓ = 8). In this work, it was found to be necessary to explore 57 dimensions (ℓ =12) to obtain comparable accuracy in the plastic properties of hexagonal polycrystals.

(iii) A new method was proposed to delineate property closures in hcp polycrystals. This method essentially builds closures in an iterative approach by considering weighted combinations of the textures that produce property combinations on the boundary of the closure. This method was successfully used here to produce several examples of elastic-plastic property closures in hexagonal-orthorhombic textures (using previously established slip-system level properties of high purity and commercially pure α-Ti).

CHAPTER5: CONCLUSIONS AND FUTURE WORK

5.1. Conclusions

1. This thesis provided a novel and efficient framework for modeling the anisotropic stress-strain response and texture evolution at large plastic deformation in α-titanium alloys at ambient temperature. Crystallographic slip, deformation twinning and slip inside twinning have been all incorporated in the model as important mechanisms for accommodating plastic deformation. Grain-fragmentation scheme was proposed to facilitate the formulation of strain hardening functions which reflect the complex slip-twin interactions and overcome the obstacles which are mainly caused by the large number of new orientations produced by twinning.

2. The complex slip-twin hardening functions have been further improved from their previous versions by allowing different hardening parameters for different slip and twin families. This improvement has been observed to provide better predictions in both texture evolution and stress-strain responses in a number of deformation paths, without requiring a significant increase of computation cost.

3. The accuracy of the proposed framework was evaluated quantitatively by direct comparisons with experimental measurements in high purity and commercial purity α-titanium. The modeling predictions showed close agreement with measurements for both materials in stress-strain behavior and texture evolution.

The effects of Taylor assumption on the modeling prediction were careful evaluated by comparing the stress and strain distributions with finite element framework as a function of plastic anisotropy (in this work plastic anisotropy is defined as the ratio of critical resolved shear stresses among different slip families).

4. A new computational scheme for delineating the comprehensive elastic-plastic property closures for hexagonal close-packed polycrystal using the spectral framework of MSD was provided in this thesis. For the first time in literature, MSD framework has been applied to hcp metals for constructing a variety of elastic-plastic property closures. Especially, an expanded elastic-plastic closure for mechanically processed α-titanium from annealed to heavily cold-wrought microstructures was depicted. Moreover, an extremely useful property closure (R-σ_{y1}) for metals processing community was defined and then delineated.

5.2. Future Work

1. The materials investigated in this work are limited to single phase, pure titanium with average grain size about 30um and ambient temperature. In order to expand the proposed crystal plasticity model and MSD framework to a broader range of applications, further experimental studies are needed to characterize the microstructures of the materials of interest.

2. The effects of Taylor assumption on modeling prediction have been evaluated in this thesis. In order to avoid such a gross simplification, the proposed crystal plasticity model should be implemented into finite element framework.

3. In the current study of MSD, the primary focus is on the delineation of property closures for a given material at certain microstructures. The accuracy of the property closures is limited due to the use of first-order bounding theories. The higher-order homogenization theories are needed to overcome this problem.

List of References

1 Semlitsch M, Staub F, Weber H. Development of a vital, high-strength titanium-aluminium-niobium alloy for surgical implants. Advances in Biomaterials 1986:69.

2 Hanson BH. Present and future uses of titanium in engineering Materials & Design 1986;7:301.

3 Fores FH, Allen PG, Niinomi M. Non-aerospace implications of titanium - an overview. Proc of Symposium on Non-Aerospace Applications of Titanium. San Antonio, Texas, 1998.

4 Santhanam AT, Reed-Hill RE. The influence of strain rate dependent work hardening on the necking strain in α-titanium at elevated temperatures. Metall Trans 1971;2:2619.

5 Nourbakhsh S, O'Brien TD. Texture formation and transition in cold-rolled titanium Materials Science and Engineering 1988;100:109.

6 Gray III GT. Influence of strain rate and temperature on the structure, property behavior of high-purity titanium. Journal De Physique IV 1997;Colloque C3:423.

7 Nemat-Nasser S, Guo WG, Cheng JY. Mechanical properties and deformation mechanisms of a commercially pure titanium. Acta Materialia 1999;47:3705.

8 Salem AA, Kalidindi SR, Doherty RD, Semiatin SL. Strain hardening due to deformation twinning in α-titanium: Mechanisms. Metall Trans A 2006;37A:259.

9 Partiridge PG. Metallurgia Revised 1967;12:169.

10 Christian JW, Mahajan S. Deformation twinning. Progress in Materials Science 1995;39:1.

11 Nemat-Nasser S, Guo WG, Cheng JY. Acta Materialia 1999;47:3705.

12 Garde AM, Reed-Hill RE. Metall Trans A 1971;2:2885.

13 Salem AA, Kalidindi SR, Doherty RD. Strain hardening of titanium: role of deformation twinning. Acta Materialia 2003;51:4225.

14 Kothari M, Anand L. Elasto-viscoplastic constitutive equations for policrystalline metals: application to tantalum. Journal of the Mechanics and Physics of Solids 1998;46:51.

15 Kalidindi SR, Bronkhorst CA, Anand L. Crystallographic Texture Evolution in Bulk Deformation Processing of Fcc Metals. Journal of the Mechanics and Physics of Solids 1992;40:537.

16 Asaro RJ. Crystal Plasticity. Journal of Applied Mechanics 1983;50:921.

17 Asaro RJ, Needleman A. Texture development and strain hardening in rate dependent polycrystals. Acta Metallurgica et Materialia 1985;33:923.

18 Mathur KK, Dawson PR. On modelling the development of crystallographic texture in bulk forming processes. International Journal of Plasticity 1989;5:67.

19 Myagchilov S, Dawson PR. Materials Science and Engineering A 1999;7:975.

20 Phillipe MJ, Serghat M, Van Houtte P, Esling C. Acta Metallurgica et Materialia 1995;43:1619.

21 Balasubramanian S, Anand L. Acta Materialia 2002;50:133.

22 Kalidindi SR. Incorporation of deformation twinning in crystal plasticity models. Journal of the Mechanics and Physics of Solids 1998;46:267.

23 Salem AA, Kalidindi SR, Semiatin SL. Strain hardening due to deformation twinning in α-titanium: Constitutive relations and crystal-plasticity modeling Acta Materialia 2005;53:3495.

24 Adams BL, Henrie A, Henrie B, Lyon M, Kalidindi SR, Garmestani H. Microstructure-sensitive design of a compliant beam. Journal of the Mechanics and Physics of Solids 2001;49:1639.

25 Lyon M, Adams BL. Gradient-based non-linear microstructure design. Journal of the Mechanics and Physics of Solids 2004;52:2569.

26 Kalidindi SR, Houskamp JR, Lyons M, Adams BL. Microstructure sensitive design of an orthotropic plate subjected to tensile load. International Journal of Plasticity 2004;20:1561.

27 Cherkaev A. Variational Methods for Structural Optimization. New York: Springer, 2000.

28 Proust G, Kalidindi SR. Procedures for construction of anisotropic elasti-plastic property closures for face-centered polycrystals using first order bouding relations. Journal of the Mechanics and Physics of Solids 2006;54:1744.

29 Singh RP, Doherty RD. Strengthening in MULTIPHASE (MP35N) alloy - Ambient temperature deformation and recrystallization. Metallurgical Transactions A 1992;23:307.

30 El-Danaf E, Kalidindi SR, Doherty RD. Influence of deformation path on the strain hardening behavior and microstructure evolution in low SFE FCC metals. International Journal of Plasticity 2001;17:1245.

31 Van Houtte P. Simulation of the rolling and shear texture of brass by the Taylor theory adapted for mechanical twinning. Acta Metallurgica et Materialia 1978;26:591.

32 Tome CN, Lebensohn RA, Kocks UF. A model for texture development dominated by deformation twinning: Application to zirconium alloys. Acta Metall 1991;39:2667.

33 Staroselsky A, Anand L. Inelastic deformation of polycrystalline face centered cubic materials by slip and twinning. Journal of the Mechanics and Physics of Solids 1998;46:671.

34 Staroselsky A, Anand L. A constitutive model for hcp materials deforming by slip and twinning: application to magnesium alloy AZ31B International Journal of Plasticity 2003;19:1843.

35 Kaschner GC, Tome CN. Role of twinning in the hardening response of zirconium during temperature reloads Acta Materialia 2006;02:36.

36 Bunge HJ. Texture analysis in materials science. Mathematical methods. Gottingen: Cuvillier Verlag, 1993.

37 Kalidindi SR. Modeling anisotropic strain hardening and deformation textures in low stacking fault energy fcc metals. International Journal of Plasticity 2001;17:837.

38 Gurtin ME. An introduction to continuum mechanics. New York: Academic Press, 1981.

39 Asgari S, El-Danaf E, Kalidindi SR, Doherty RD. Strain hardening regimes and microstructural evolution during large strain compression of low stacking fault energy fcc alloys that form deformation twins. Metallurgical and Materials Transactions A: Physical Metallurgy and Materials Science 1997;28A:1781.

40 Taylor GI. Plastic strain in metals. Journal of the Institute of Metals 1938;62:307.

41 Paton NE, Williams JC. The deformation of α-phase titanium Titanium Science and Technology 1973;2:1049.

42 Song SG, Gray III GT. Structural interpretation of the nucleation and growth of deformation twins in Zr and Ti--II. Tem study of twin morphology and defect reactions during twinning. Acta Metallurgica et Materialia 1995;43:2339.

43 Salem AA, Kalidindi SR, Doherty RD. Strain hardening regimes and microstructure evolution during large strain compression of high purity titanium. Scripta Materialia 2002;46:419.

44 Kallend JS, Kocks UF, Rollett AD, Wenk HR. Operational texture analysis. Materials Science & Engineering A: Structural Materials: Properties, Microstructure and Processing 1991;A132:1.

45 Gil Sevillano J, Van Houtte P, Aernoudt E. Large strain work hardening and textures. Progress in Materials Science 1980;25:69.

46 Bronkhorst CA, Kalidindi SR, Anand L. Polycrystalline plasticity and the evolution of crystallographic texture in FCC metals. Philosophical Transactions of the Royal Society of London Series a-Mathematical Physical and Engineering Sciences 1992;341:443.

47 Hirsch J, Lucke K. Mechanism of deformation and development of rolling textures in polycrystalline FCC metals - I. Description of rolling texture development in homogeneous CuZn alloys. Acta Metallurgica et Materialia 1988;36:2863.

48 Paul B. Prediction of elastic constants of multiphase materials. Trans. Metall. Soc. AIME 1960:36.

49 Hill R. The elastic behavior of a crystalline aggregate. Proceedings of the Royal Society of London. Series A, Mathematical and Physical Sciences 1952;65:349.

50 Hill R. Elastic properties of reinforced solids: some theoretical principles. Journal of the Mechanics and Physics of Solids 1963;11:357.

51 Avellaneda M, Cherkaev AV, Gibiansky LV, Milton GW, Rudelson M. A complete characterization of the possible bulk and shear moduli of planar polycrystals. Journal of the Mechanics and Physics of Solids 1996;44:1179.

52 Hashin Z, Shtrikman S. Note on a variational approach to the theory of composite elastic materials. Journal of the Franklin Institute 1961;271:336.

53 Hashin Z, Shtrikman S. A variational approach to the theory of the elastic behaviour of polycrystals. Journal of the Mechanics and Physics of Solids 1962;10:343.

54 Hashin Z, Shtrikman S. A variational approach to the theory of the elastic behaviour of multiphase materials. Journal of the Mechanics and Physics of Solids 1963;11:127.

55 Kröner E. Bounds for effective elastic moduli of disordered materials. J. Mech. Phys. Solids 1977;25:137.

56 Beran MJ, Mason TA, Adams BL, Olsen T. Bounding elastic constants of an orthotropic polycrystal using measurements of the microstructure. Journal of the Mechanics and Physics of Solids 1996;44:1543.

57 Adams BL, Olson T. The mesostructure - properties linkage in polycrystals. Progress in Materials Science 1998;43:1.

58 Brown WF. Solid mixture permittivities. The Journal of Chemical Physics 1955;23:1514.

59 Beran MJ. Stattistical Continuum Theories. John Wiley & Sons, Interscience, New York, NY 1968.

60 Torquato S. Random Heterogeneous Materials. New York: Springer-Verlag, 2002.

61 Fullwood DT, Adams BL, Kalidindi SR. Generalized pareto front methods applied to second-order material property closures. Computational Materials Science 2006;In press.

62 Kim IY, de Weck OL. Adaptive weighted-sum method for bi-objective optimization: Pareto front generation. Structural and Multidisciplinary Optimization 2005;29:149.

63 Knezevic M, Kalidindi SR. Fast computation of first-order elastic-plastic closures for polycrystalline cubic-orthorhombic microstructures. Computational Materials Science 2006;In press.

64 Sachs G. Zur Ableitung einer Fließbedingung. Z. Ver. Deu. Ing. 1928;72:734.

65 Press WH, Teukolsky SA, Vetterling WT, Flannery BP. Numerical recipes in C++, 2002.

66 Wu X, Kalidindi SR, Necker C, Salem AA. Prediction of crystallographic texture evolution and anisotropic stress-strain curves during large plastic strains in high purity α-titanium using a Taylor-type crystal plasticity model Acta Materialia 2006;In press.

APPENDIX A: FIGURES

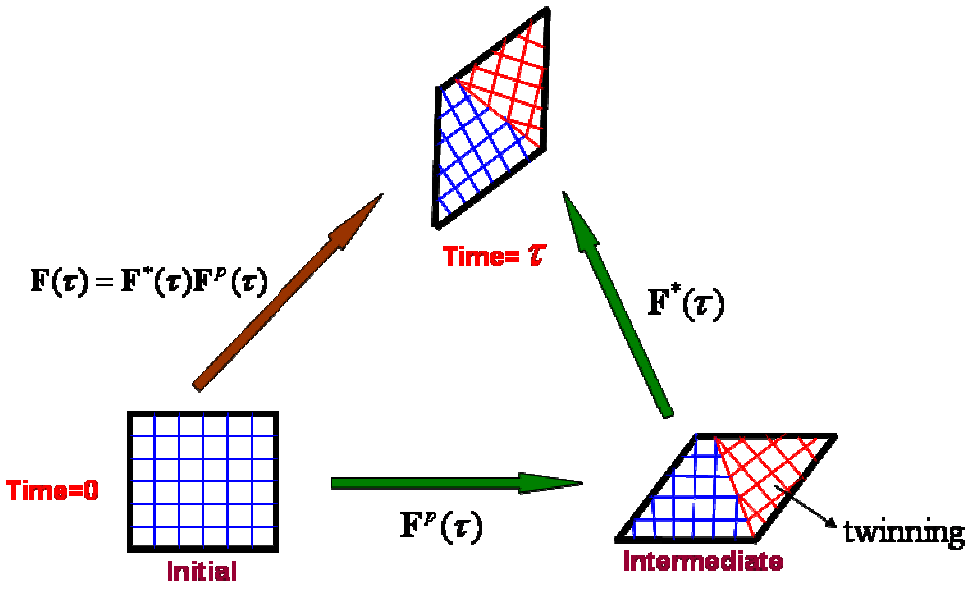

Figure 1. A schematic of the interpretation of the multiplicative decomposition of deformation gradient when twinning is included.

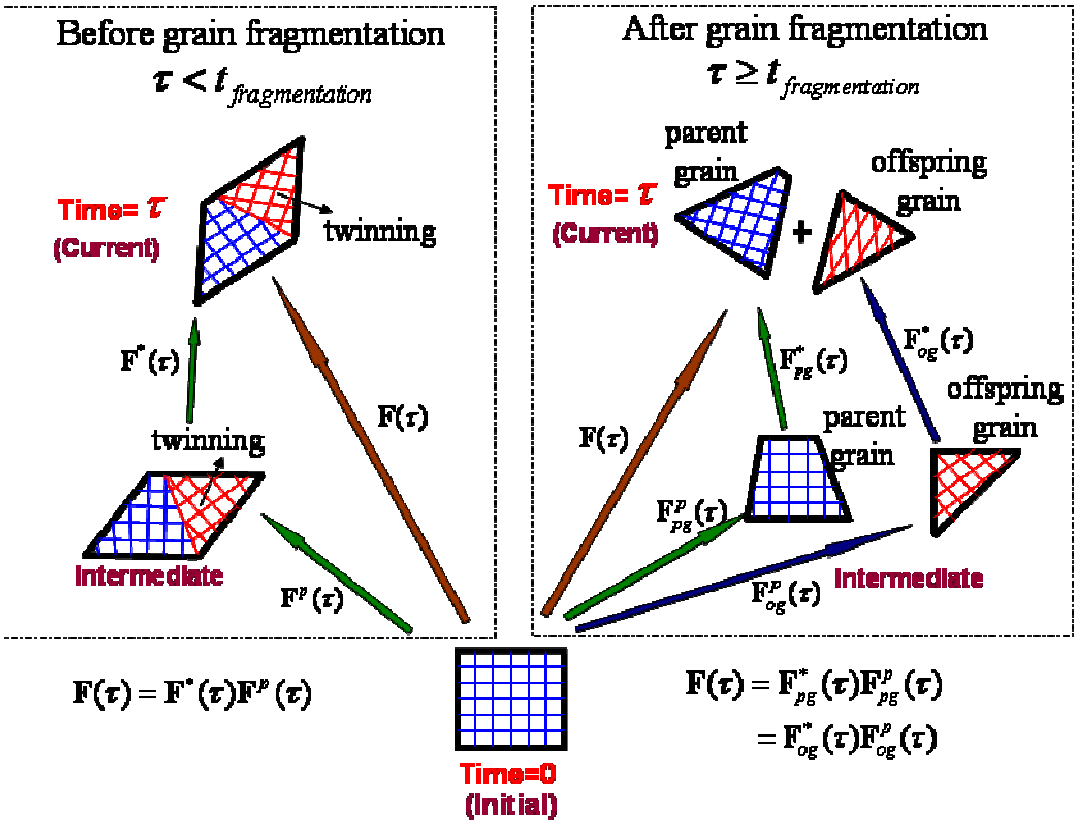

Figure 2. Summary of the multiplicative decomposition of the total deformation gradient implemented in the proposed model. *pg* denotes the parent grain and *og* denotes the offspring grain. Only one offspring is shown in the figure for clarity.

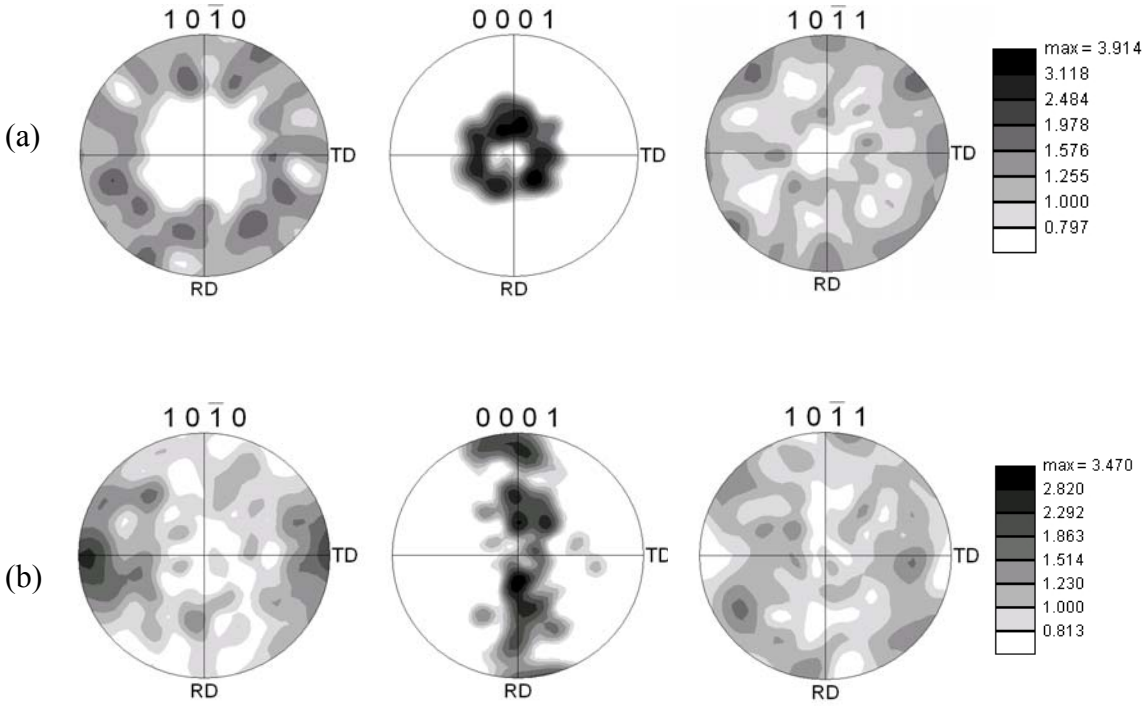

Figure 3. Initial textures of (a) high purity and (b) commercial purity α-titanium samples.

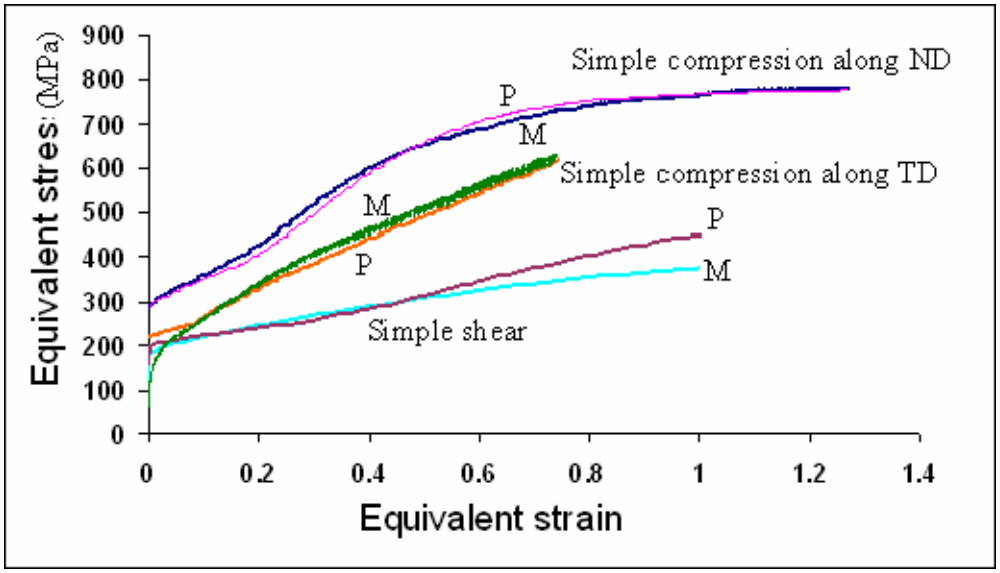

Figure 4. Comparison of predicted (P) and measured (M) equivalent stress-equivalent strain curves for different deformation modes on high purity α-Ti.

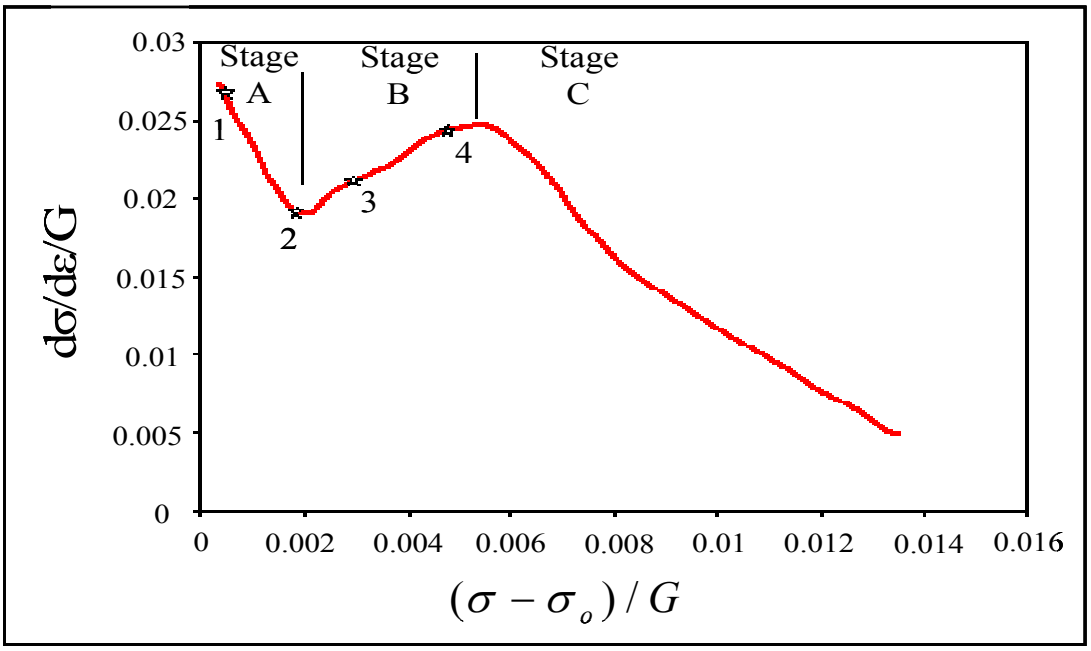

Figure 5. Strain hardening response of high purity α-Ti in simple compression along ND. The ordinate is the normalized slope of the stress-strain curve and the abscissa is the normalized plastic flow stress. G is theoretical shear modulus for titanium, and σ_o is the initial yield stress.

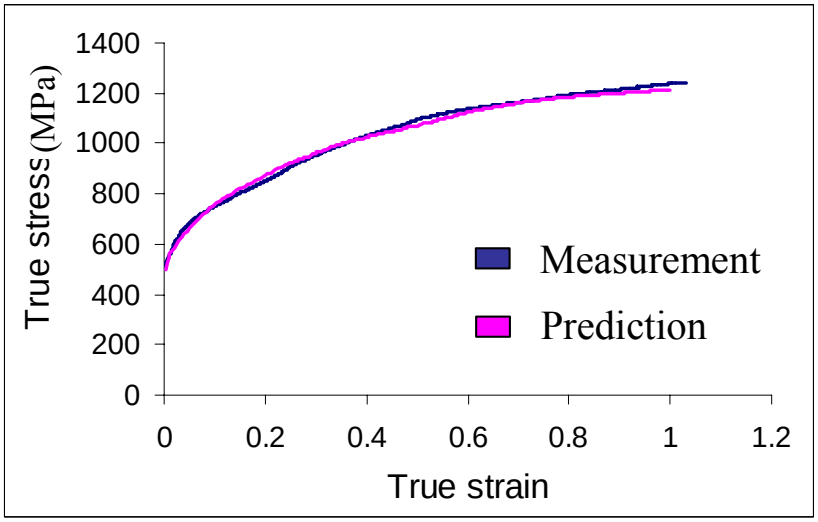
1400
1200
1000
800
600
400
200
0
True stress (MPa)
0
0.2
0.4
0.6
0.8
1
1.2
True strain
Measurement
Prediction

(a)

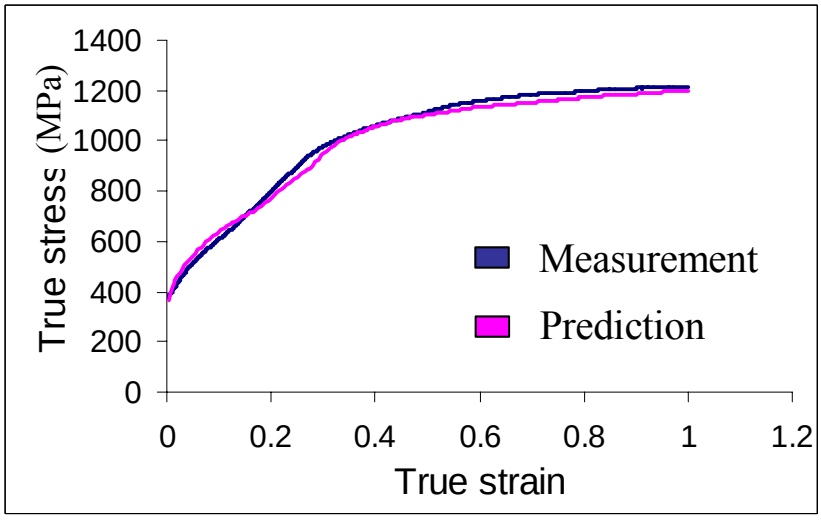
1400
1200
1000
800
600
400
200
0
True stress (MPa)
0
0.2
0.4
0.6
0.8
1
1.2
True strain
Measurement
Prediction

(b)

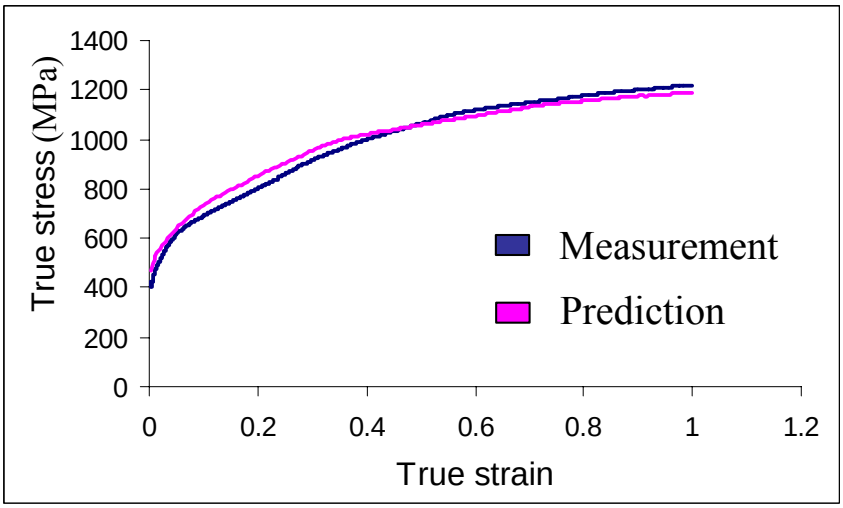

(c)

Figure 6. Comparison of predicted and measured true stress-true strain curves for different deformation modes in commercial purity α-Ti: (a) simple compression along ND, (b) simple compression along TD, and (c) simple compression along RD. Curves in (a) and (b) were used for calibration, and curves in (c) were used for evaluation.

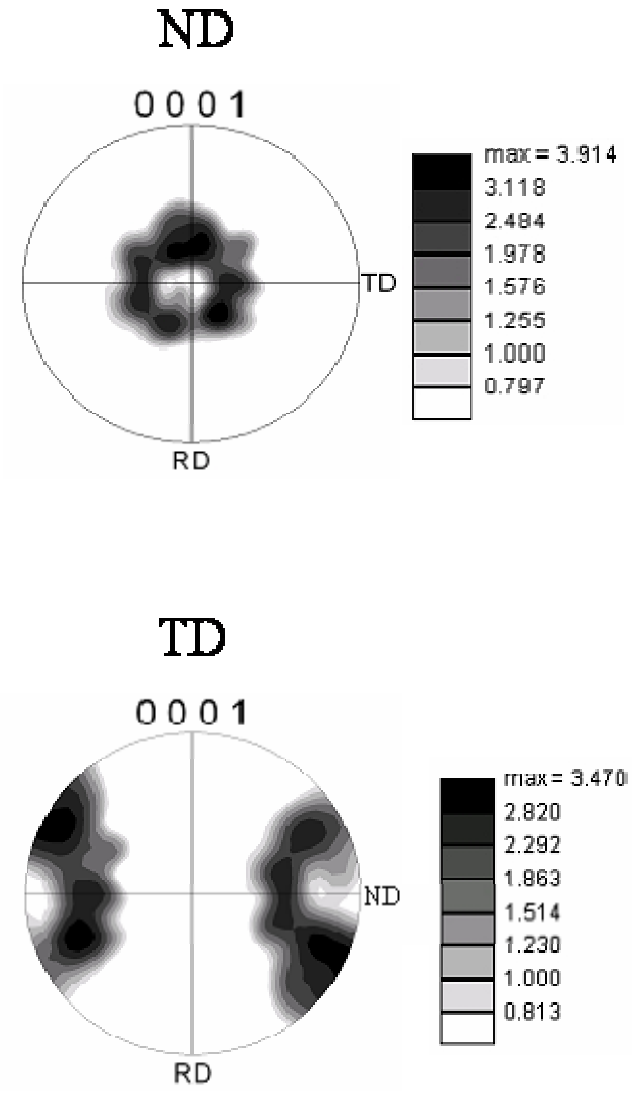

Figure 7. Comparison of initial textures for compression tests on high purity α-Ti along ND and TD.

Measurement

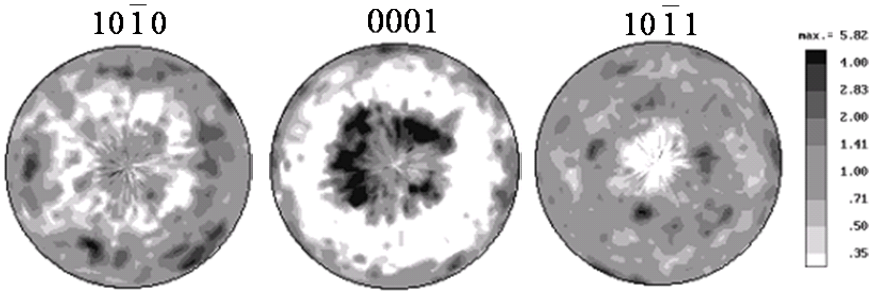

Prediction

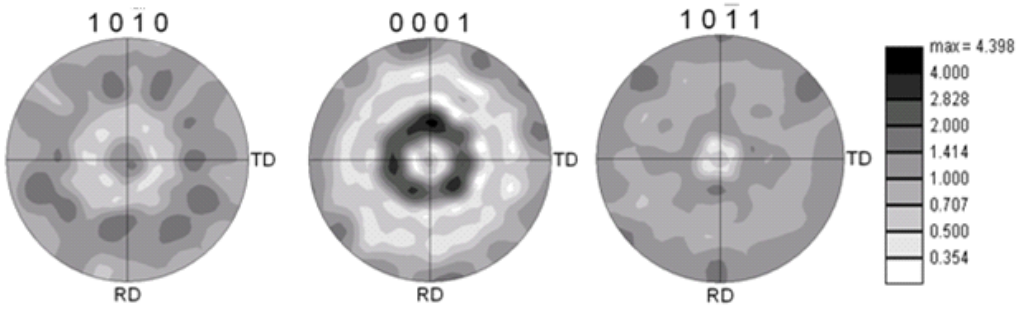

Figure 8. Comparison of predicted and measured textures at $\varepsilon = -0.22$ in simple compression of high purity α-Ti along ND.

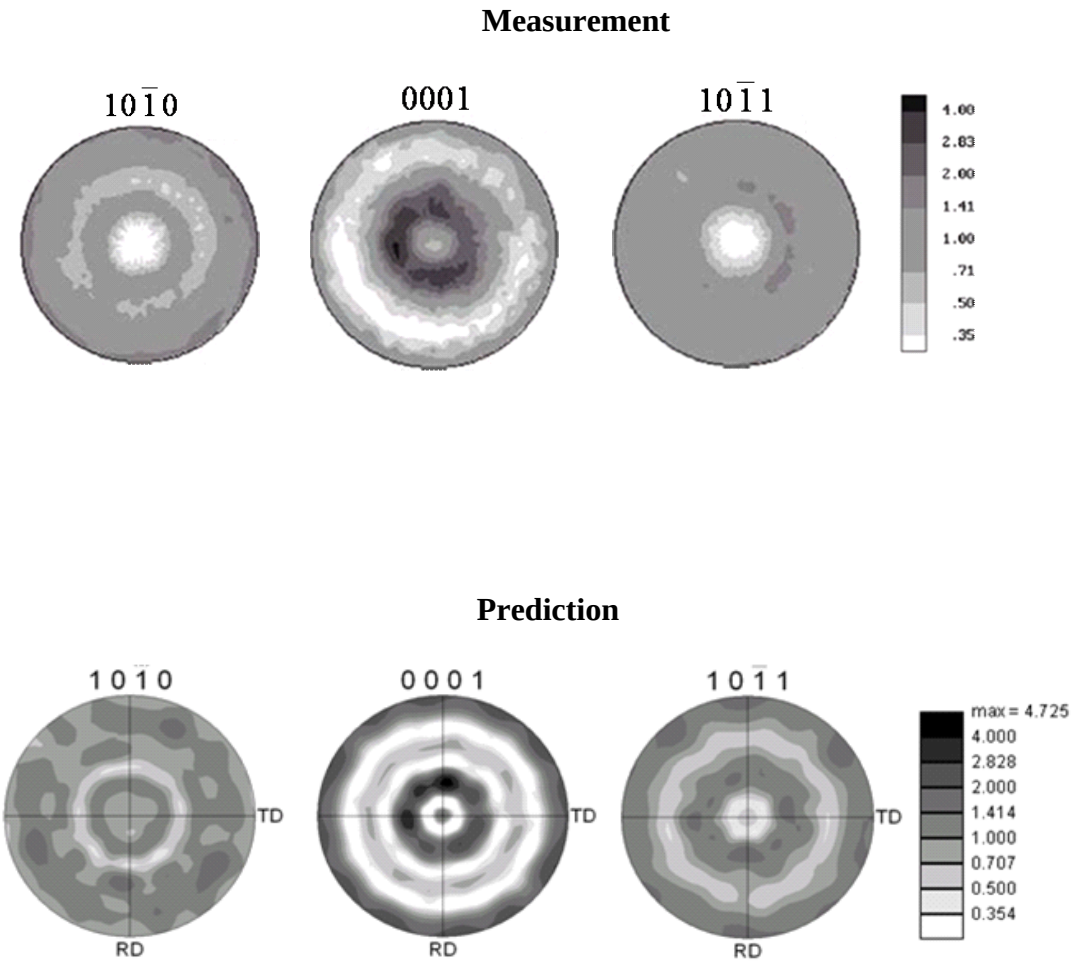

Figure 9. Comparison of predicted and measured textures at $\varepsilon = -1.00$ in simple compression of high purity α–Ti along ND.

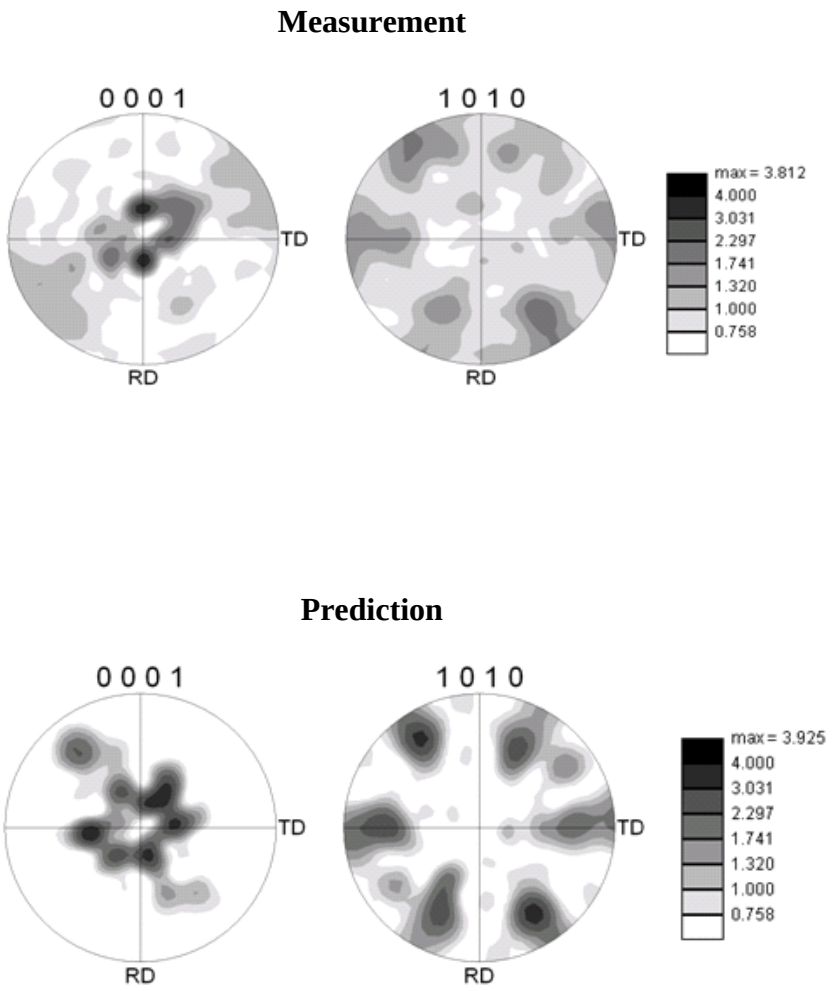

Figure 10. Comparison of predicted and measured textures at $\gamma = -1.00$ in simple shear of high purity α-Ti.

(a) Simple compression along ND

Measurement

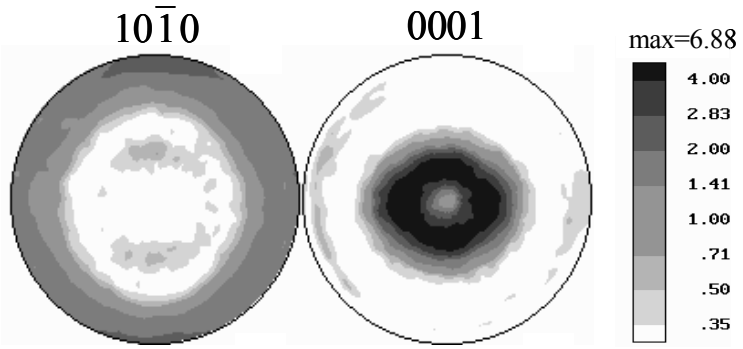

Prediction

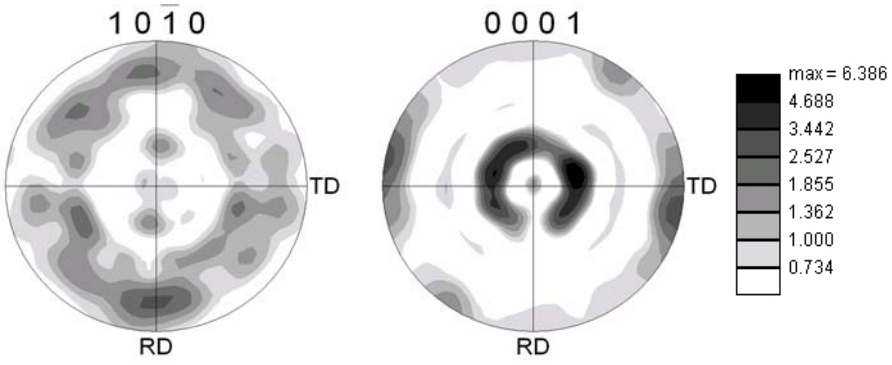

(b) Simple compression along TD

Measurement

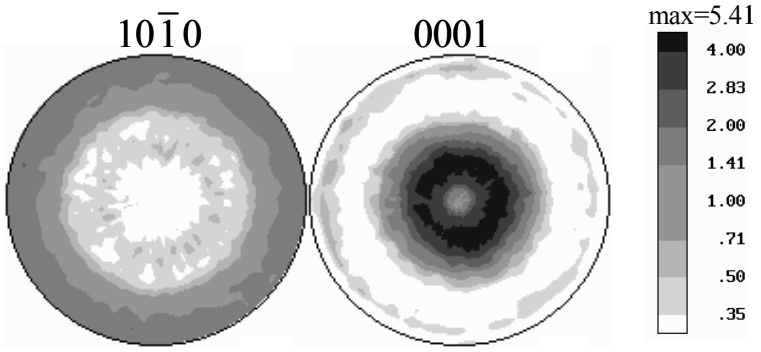

Prediction

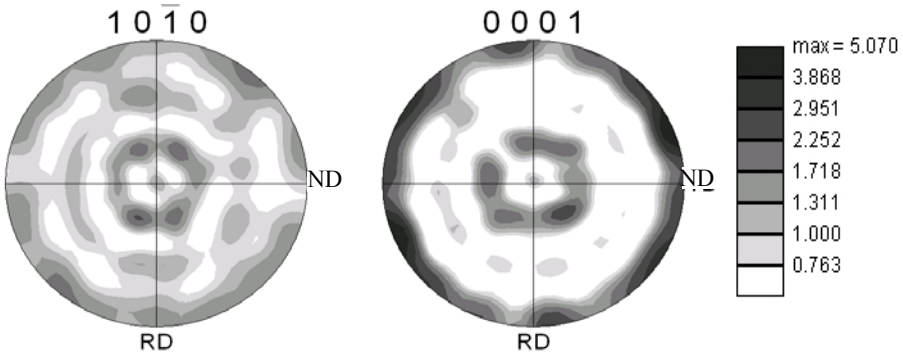

(c) Simple compression along RD

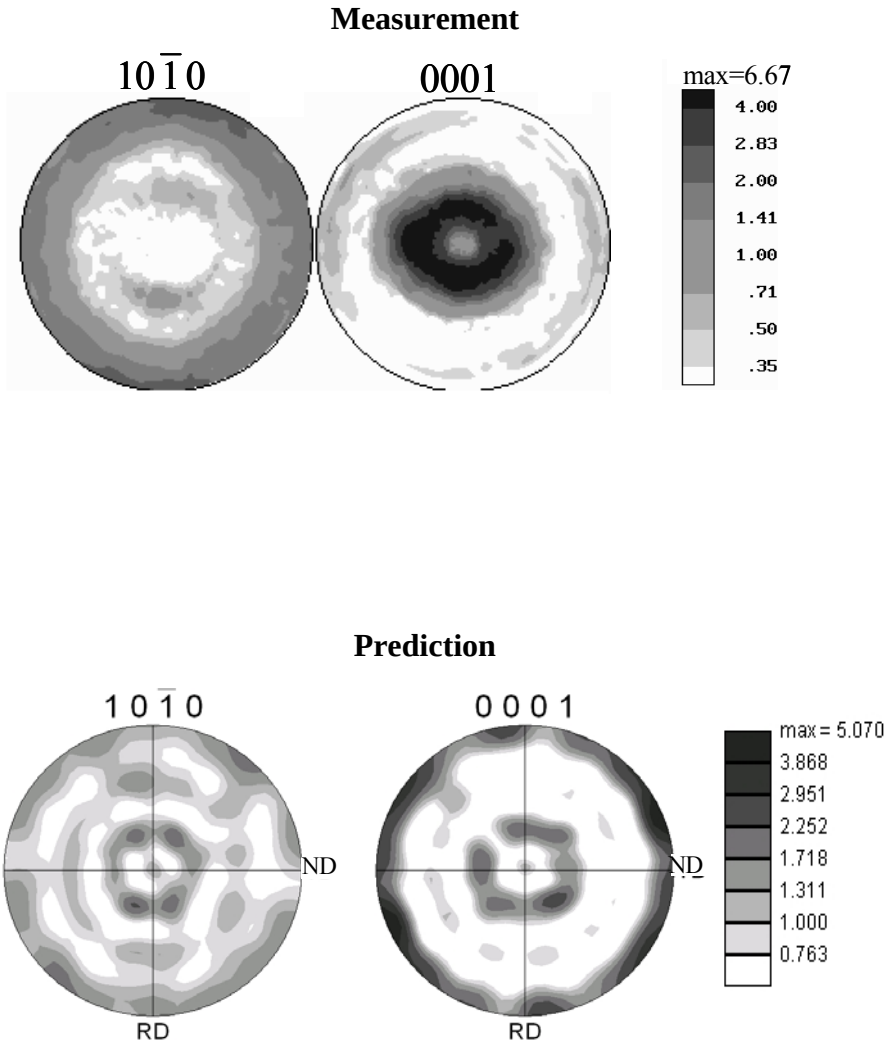

Figure 11. Comparison of predicted and measured textures at $\varepsilon = -1.0$ in simple compression tests along (a) ND, (b) TD and (c) RD for commercial purity α-titanium.

(a)

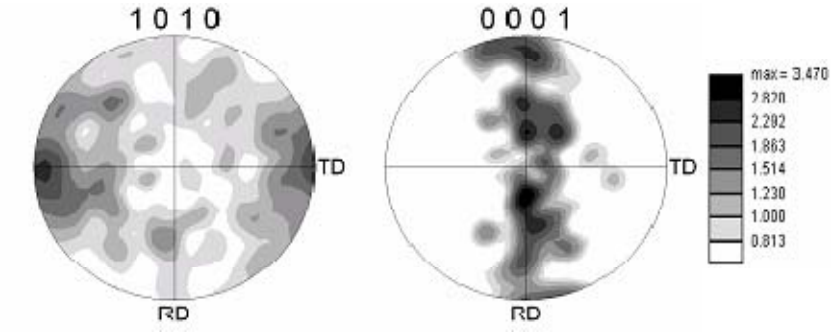

(b)

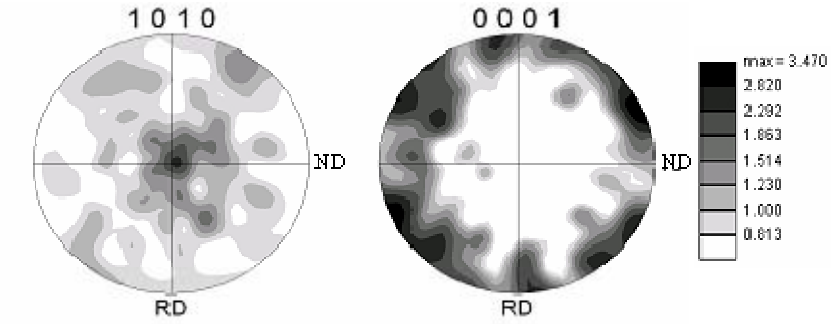

(c)

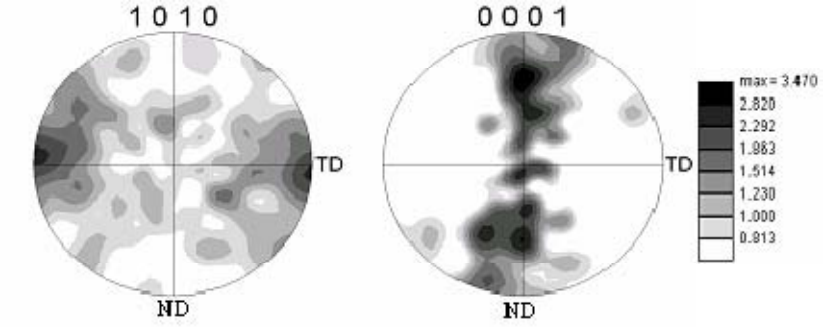

Figure 12. Comparison of initial textures along (a) ND, (b) TD and (c) RD in commercial purity α-titanium.

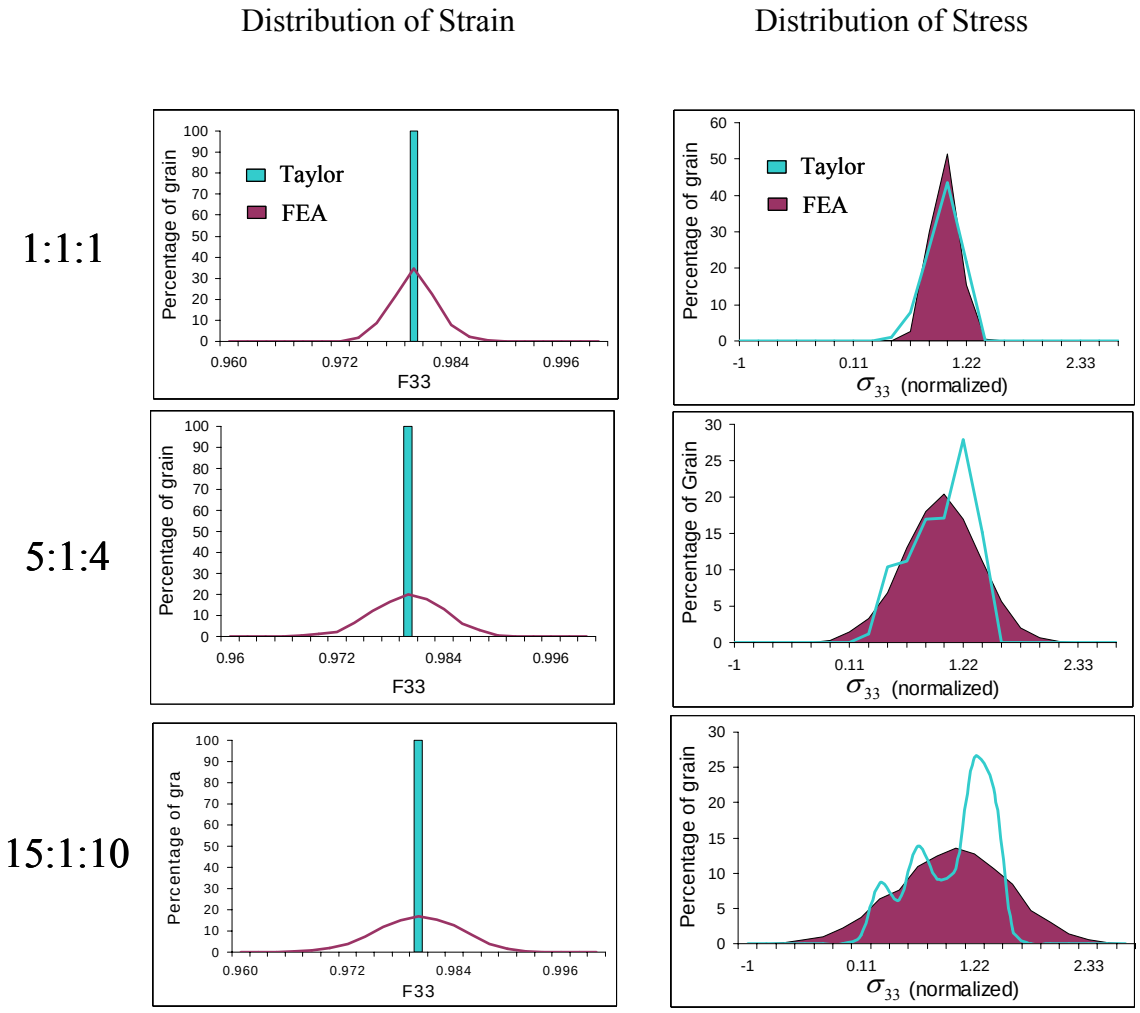

Figure 13. Comparison of predicted stress and strain distribution at small strains between Taylor model and Finite Element method as a function of plastic anisotropy (ratio of critical resolved shear stresses of selected slip families in α-titanium).

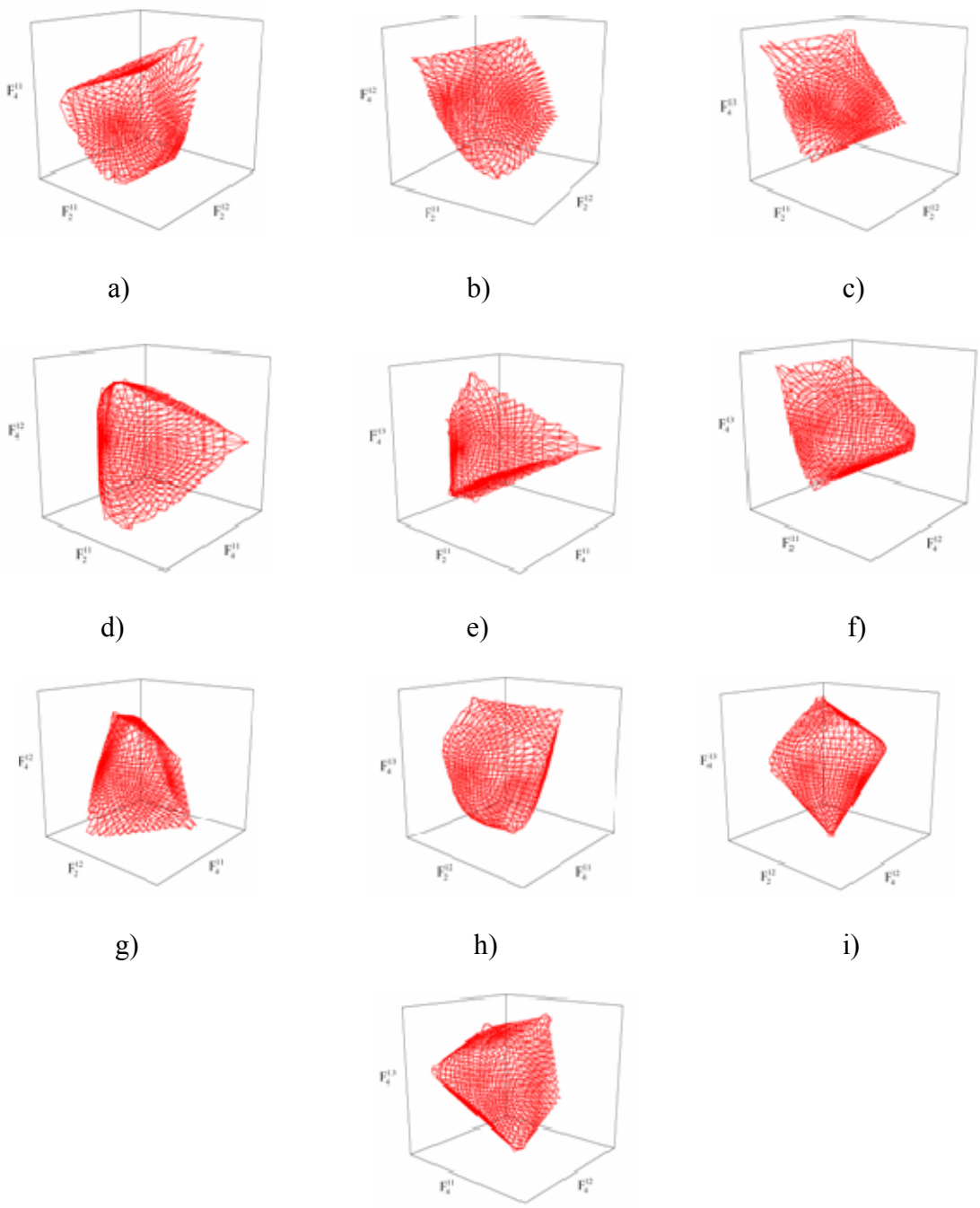

Figure 14. Thee-dimensional projections of the texture Hull for hcp-orthorhombic materials for the first five dimensions of the Fourier space. The presented sections are: a) $\left(F_2^{11}, F_2^{12}, F_4^{11}\right)$, b) $\left(F_2^{11}, F_2^{12}, F_4^{12}\right)$, c) $\left(F_2^{11}, F_2^{12}, F_4^{13}\right)$, d) $\left(F_2^{11}, F_4^{11}, F_4^{12}\right)$, e) $\left(F_2^{11}, F_4^{11}, F_4^{13}\right)$, f) $\left(F_2^{11}, F_4^{12}, F_4^{13}\right)$, g) $\left(F_2^{12}, F_4^{11}, F_4^{12}\right)$, h) $\left(F_2^{12}, F_4^{11}, F_4^{13}\right)$, i) $\left(F_2^{12}, F_4^{12}, F_4^{13}\right)$, j) $\left(F_4^{11}, F_4^{12}, F_4^{13}\right)$.

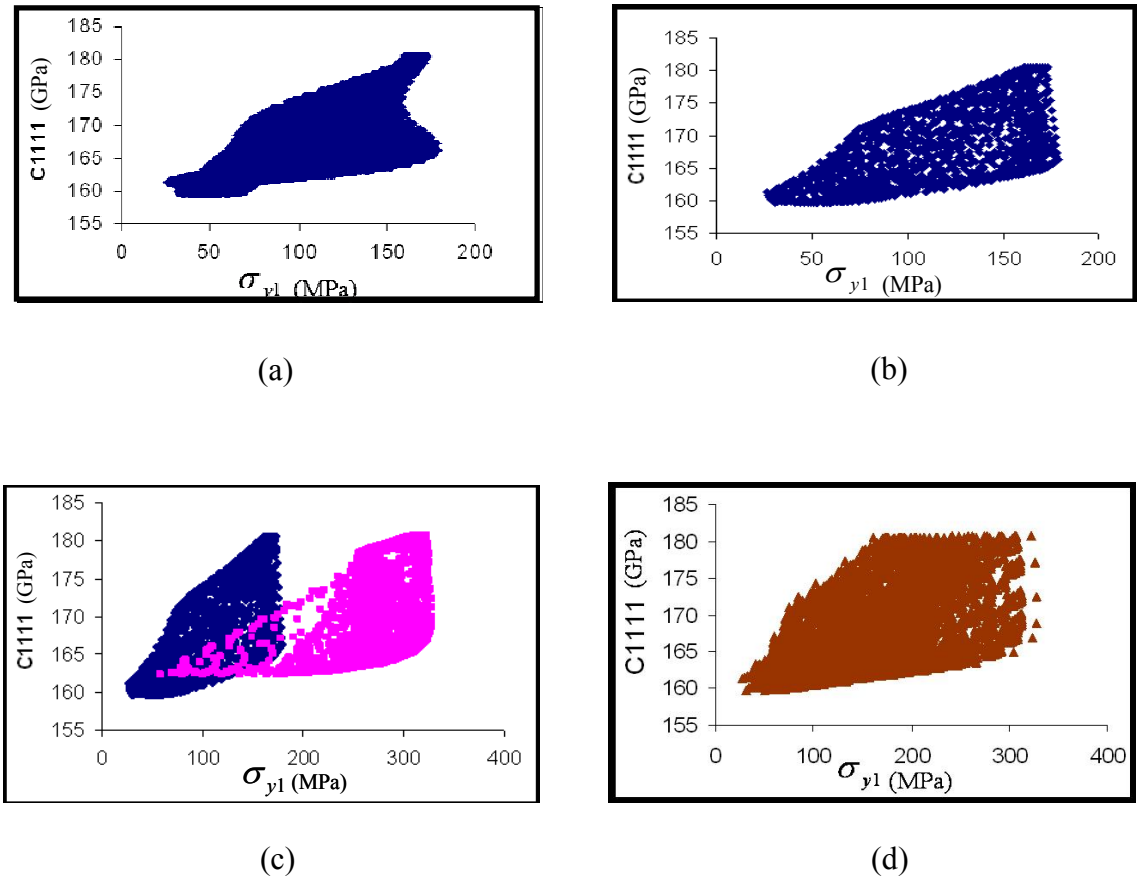

Figure 15. (σ_{y1}-C_{1111}) property closures for annealed high purity α-titanium: (a) lower bound property closure for eigen-textures, (b) the complete lower bound property closure, (c) the complete lower and upper bound property closures, and (d) the complete first-order property closure.

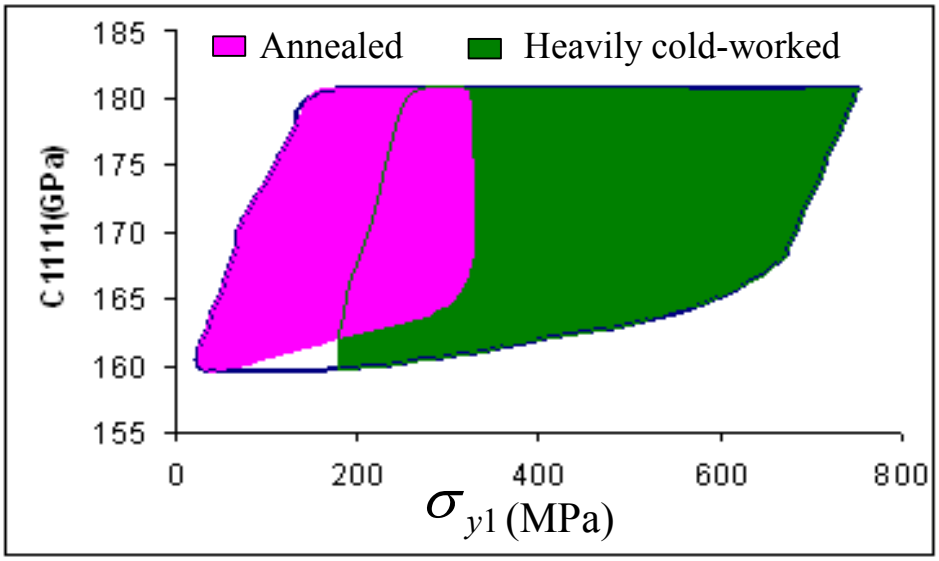

Figure 16. Complete (σ_{y1} - C_{1111}) closures for high purity α-titanium with an average initial grain size of 30 μm in two conditions: (i) annealed, and (ii) heavily cold-worked.

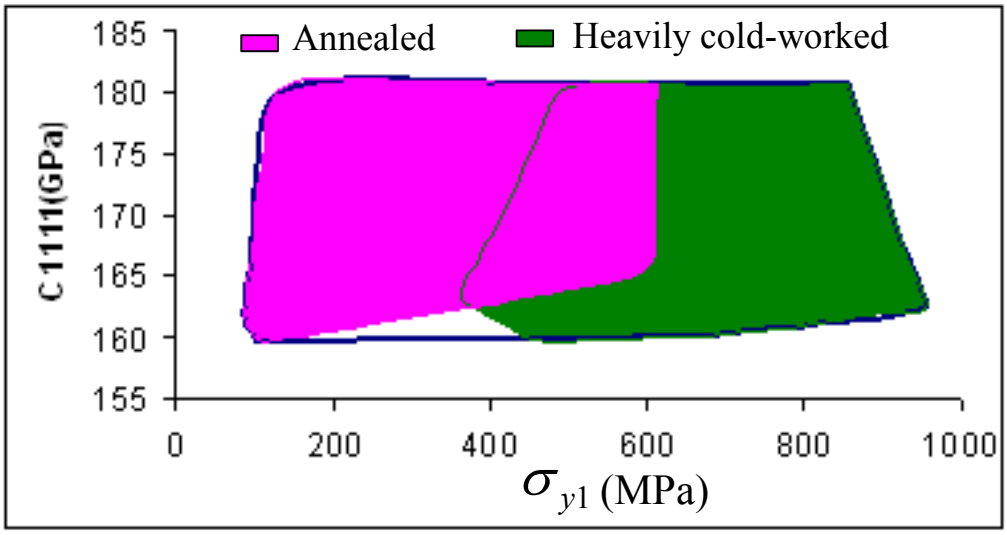

Figure 17. Complete (σ_{y1} - C_{1111}) closures for commercial purity α-titanium with an average initial grain size of 35 μm in two conditions: (i) annealed, and (ii) heavily cold-worked.

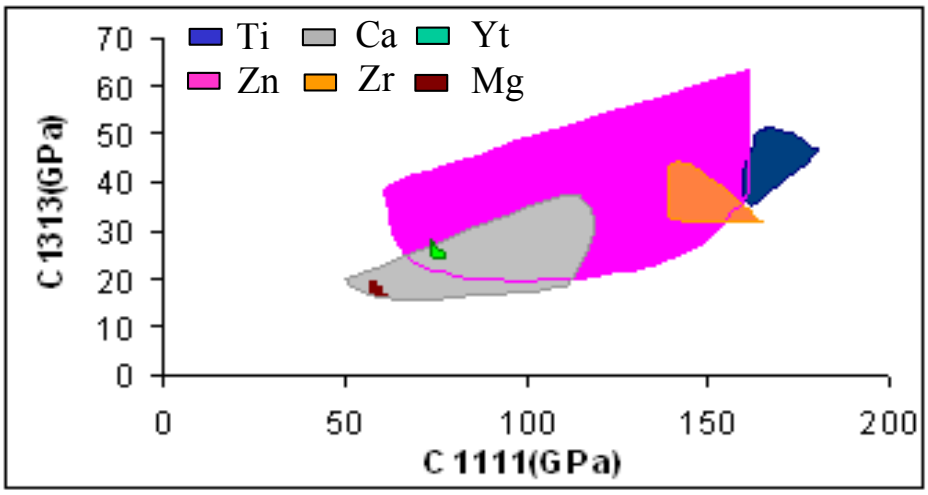

Figure 18. Complete (C_{1313} - C_{1111}) property closures for selected hexagonal polycrystals.

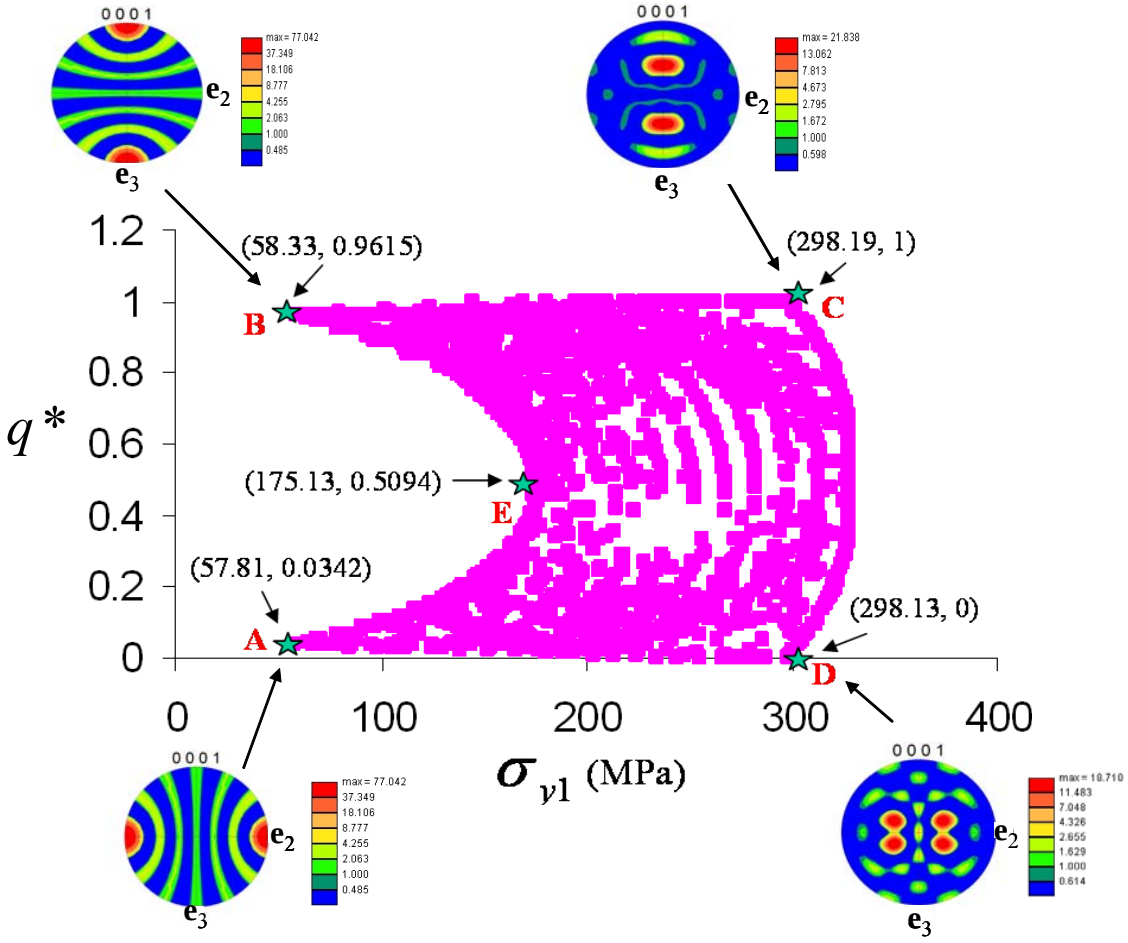

Figure 19. (q^* - σ_{y1}) property closure for annealed high purity α-titanium based on Taylor-type crystal plasticity models.

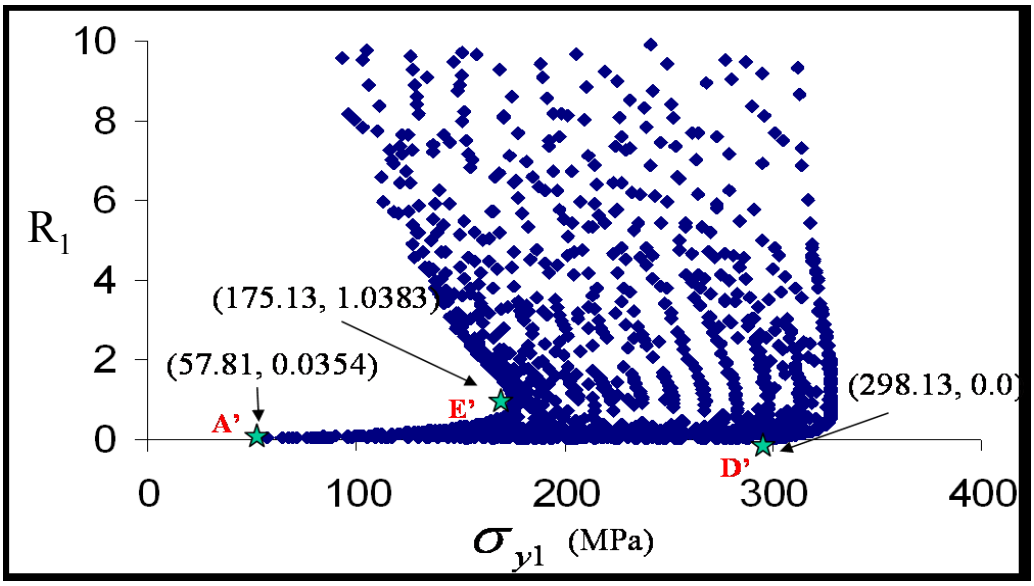

Figure 20. The truncated (R_1-σ_{y1}) closure for high purity α-titanium based on Taylor-type crystal plasticity models.

APPENDIX B: TABLES

Table1. Summary of all parameters for slip and twin systems

	Slip Systems			Twin Systems	
Family	Prismatic <a>	Basal <a>	Pyramidal <c+a>	Compressive	Tensile
Plane and direction	$\{10\bar{1}0\}$ $<11\bar{2}0>$	$\{0001\}$ $<11\bar{2}0>$	$\{10\bar{1}1\}$ $<11\bar{2}\bar{3}>$	$\{11\bar{2}2\}$ $<11\bar{2}\bar{3}>$	$\{10\bar{1}2\}$ $<10\bar{1}1>$
Number of systems	3	3	12	6	6
Initial resistance	s_o^{pri}	s_o^{bas}	s_o^{pyr}	s_{tw}^{com}	s_{tw}^{ten}
Slip hardening parameters	$h_{so}^{pri}, s_{so}^{pri}$	$h_{so}^{bas}, s_{so}^{bas}$	$h_{so}^{pyr}, s_{so}^{pyr}$	*No hardening parameters needed for twin systems.*	
Other hardening parameters	C, b, s_{spr}				

Table2. Chemical composition of α-titanium (in wppm)

Alloy	O	Fe	S	C	N	Al	Ti
CP-Ti	810	970	9	196	80	1200	Balance
HP-Ti	95	1.3	3	7	11	<1.0	Balance

Table3. Summary of estimated model parameters for high-purity titanium

Parameter	s_o^{pri}	s_o^{bas}	s_o^{pyr}	s_{tw}	$h_{so}^{pri-bas}$	h_{so}^{pyr}
Value	30MPa	150MPa	120MPa	125MPa	15MPa	300MPa
Parameter	s_{so}^{pri}	$s_{so}^{bas-pyr}$	s_{pr}	C	b	
Value	100MPa	300MPa	100MPa	25	2	

Table4. Summary of estimated model parameters for commercial-purity titanium

Parameter	s_o^{pri}	s_o^{bas}	s_o^{pyr}	s_{tw}	$h_{so}^{pri-bas}$	h_{so}^{pyr}
Value	60MPa	300MPa	240MPa	400MPa	800MPa	1500MPa
Parameter	s_{so}^{pri}	$s_{so}^{bas-pyr}$	s_{pr}	C	b	
Value	250MPa	430MPa	200MPa	30	2	

Table5. Values of Fourier coefficients for elastic stiffness components

	ℓ μ ν	C_{1111}	C_{1313}
$_{ijkl}A_\ell^{\mu\nu}$	0 1 1	0.73333	0.3
	2 1 1	0.09524	-0.07143
	2 1 2	-0.16496	-0.12372
	4 1 1	0.17144	-0.22858
	4 1 2	-0.25555	0.25555
	4 1 3	0.33806	0.00
$_{ijkl}B_\ell^{\mu\nu}$	0 1 1	0.26666	-0.13333
	2 1 1	-0.09524	-0.09524
	2 1 2	0.16498	-0.16496
	4 1 1	-0.17144	0.22857
	4 1 2	0.25555	-0.25555
	4 1 3	-0.33806	0.00
$_{ijkl}D_\ell^{\mu\nu}$	0 1 1	0.2	0.06667
	2 1 1	-0.28571	0.04762
	2 1 2	0.49487	0.08248
	4 1 1	0.08571	-0.11429
	4 1 2	-0.12778	0.12778
	4 1 3	0.16903	0.00

APPENDIX C: DOMINANT SLIP AND TWIN SYSTEMS IN α-Titanium

1. Slip systems

(i) Basal <*a*>

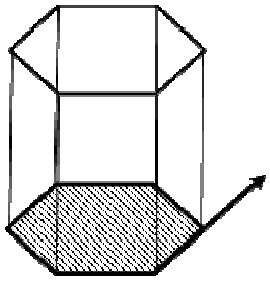

$\{0001\}<\bar{2}110>$

(ii) Prism <*a*>

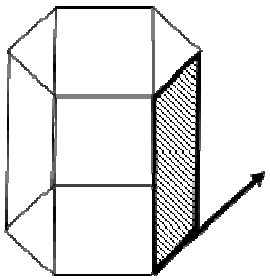

$\{10\bar{1}0\}<\bar{2}110>$

(iii) Pyramidal <*c*+*a*>

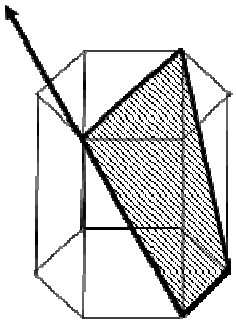

$\{10\bar{1}1\}<11\bar{2}\bar{3}>$

2. Twin systems

(i) Compressive twins

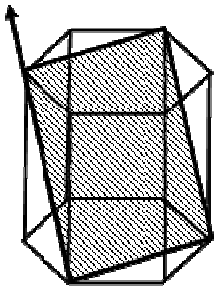

$\{10\bar{1}2\}<\bar{1}011>$

(ii) Tensile twins

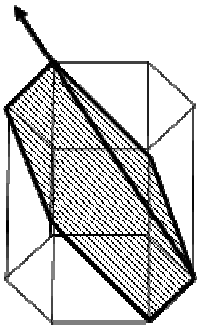

$\{11\bar{2}2\}<11\bar{2}\bar{3}>$

APPENDIX D: FORTRAN CODE FOR THE GRAIN-FRAGMENTATION SCHEME

Because of the complexity of this study, a fairly large number of non-linear equations were required to transform the simplified physical problems into numerical models which are crystal plasticity models in this study. The large amount of non-linear equations posed significant challenges for us to achieve the numerical solutions using available commercial programs. Our research group has successfully developed a numerical code in Fortran environment to solve for a number of material parameters under different mechanical processes for both cubic and hexagonal polycrystals. In the past four years, I have been largely involved in extending the previous version of Fortran code to compute anisotropic stress-strain responses and texture evolution at large strains in α-titanium by incorporating deformation twinning and slip inside twins as additional deformation mechanisms.

The subroutines attached in the following pages are parts of the Fortran code that is currently used for crystal plasticity models: one is the main program and the other is the subroutine for updating variables for offspring and parent grains. Note that the lines starting with 'C' are comments.

```
C   THIS PROGRAM IMPLEMENTS A NEW FULLY IMPLICIT TIME
INTEGRATION SCHEME
C   FOR A SET OF CONSTITUTIVE LAWS THAT DESCRIBE THE EVOLUTION
OF CRYSTAL-
C   LOGRAPHIC TEXTURE WITH LARGE DEFORMATIONS.
C
C   THIS PROGRAM IS LIMITED TO HOMOGENEOUS DEFORMATIONS.
C
C   THE DEFINITIONS OF MOST VARIABLES ARE PROVIDED IN
COMMONS.TEX.
C   THIS IS THE MAIN PROGRAM. THE LOCAL VARIABLES ARE DEFINED AS:
C
C   TEXFLAG   : A TIME FLAG INDICATING WHEN TEXTURE IS TO BE
OUTPUT.
C
C   OUTFLAG   : A TIME FLAG INDICATING WHEN STRESSES ARE TO BE
WRITTEN
C             TO FILES.
C
                                PROGRAM MAIN
C
                                INCLUDE 'commons.tex'

                                OPEN(UniT=12,FILE='SS-12.txt')
                                OPEN(UNIT=13,FILE='ND-s33.txt')
                                OPEN(UNIT=51,FILE='RD-S11.txt')
                                OPEN(UNIT=92,FILE='TD-s22.txt')
                                OPEN(UNIT=9,FILE='9-miscinfo.txt')
                                OPEN(UNIT=35,FILE='texture-OIM.txt')
                                OPEN(UNIT=36,FILE='STRAIN-FTW.txt')
                                OPEN(UNIT=37,FILE='TWINSYSTEM.txt')
                                OPEN(UNIT=55,FILE='CHECK.txt')

                                 CALL INPUT

                                 CALL INITIALIZE

                                TEXFLAG = TEX
                                OUTFLAG = TAUTO
                                NCHILD = ZERO

c     assign iflag=zero to all grains at beginning

                                DO KLM=1,NCRYS
                                  VFRAC(KLM)=1.0
                                  IFLAG(KLM)=ZERO
```

```
                                ENDDO

C     START OF TIME LOOP

100   IF(TIME.EQ.TTIME)GO TO 300
                                TAU = TIME + DTIME

                                IF(TAU.GT.TTIME)THEN
                                  TAU = TTIME
                                  DTIME = TAU - TIME
                                ENDIF
                                WRITE(*,*)'TAU=',TAU

C     GET THE DEFORMATION GRADIENT AT TAU IN GLOBAL COORDINATES

                                CALL DEFGRAD

C   START OF LOOP OVER CRYSTALS
c     note: 'ncrys' has been updated at the end of last time increment

                                DO 200 ICRYS = 1,ncrys

c     Once the grain is fragmented, twin volume fraction of offspring grain is setted
c     to be zero in the rest of deformation.
c     So we don't need to calculate twin volume fraction anymore, that's why we set
c      ntwin=zero

      IF(IFLAG(ICRYS).NE.ZERO) THEN
                                 NTWINTEMP=NTWIN
                                 NTWIN=ZERO
      ENDIF

C     COMPUTE THE TRIAL STRESS TBTR
                                CALL TRSTRESS(ICRYS)
C
C     SOLVE FOR TBTAU; USE TBTMAT AS INITIAL GUESS
C
                                DO 310 J=1,3
                                DO 310 K=1,3
310         TBTAU(J,K,ICRYS) = TBTMATT(J,K,ICRYS)

C      Update Delta gamma and CRSS on each slip or twin system
c      The new slip-twin hardening functions are formed in this subroutine
c      Two-level loops of the iterative procedrue were applied here to ensure that
c      a proper increment is achieved.
```

```
                              CALL NEWT(ICRYS)

c     Update all the required variables for next time step
c     Cauchy stress is computed in this subroutine

                              CALL UPDATE(ICRYS)

c     Use 'iflat' to decide whether a grain is an offspring one or parent one.

                              IF(IFLAG(ICRYS).NE.ZERO) NTWIN=NTWINTEMP

200   CONTINUE


c     calculate averaged stress and twin volume fraction for aggregate

      call updatepoly

c     Output averaged stress-strain response and averaged twin volume fraction
c     Note that compressive and tensile twins are presented seperately here.

                              WRITE(36,245)-
EDOT*TAU,AVGFTW,AVGFTWTEN,AVGFTWCOM
245   FORMAT(4F12.3)

c     To justify if the deformed texture should be outputed at this point

                              IF(TAU.GE.TEXFLAG)THEN

                                                  CALL TEXTURE
                                                  TEXFLAG =
TEXFLAG+TEX
                              ENDIF

C     TO justify if stress-strain response (not the deviatoric stress) should
c     be outputed at this point

                              IF(TAU.LT.TAUTO.OR.TAU.GE.OUTFLAG) CALL
OUTPUT
                              IF(TAU.GE.OUTFLAG) OUTFLAG = OUTFLAG+OUT

C     Update time

                              TIME = TAU

c     Adjust time step
```

```
                              IF(TAU.GT.TAUTO)THEN
c                               DTIME=DTMAX
                                                    DTIME =
DTIME*0.05/DGMAXG

                              IF(DTIME.GT.DTMAX)DTIME = DTMAX
                              ENDIF

C     UPDATE VARIABLES FOR NEW GRAINS including offspring and parent grains.
Note that
c     the number of total grains is updated there.

     DO 400 ICRYS=1,NCRYS
                               IF(FTWCRYST(ICRYS).GE.FTWSAT) THEN
                                 CALL NEWGRAINS(ICRYS)
       NCRYS=NCRYS+NTWINDOM(ICRYS)
                               ENDIF
400   CONTINUE

                              GO TO 100

300                           continue

c     The end of the loop

c     Check if the number of total grains equalts to the sum of offspring and parent
c     grains.
     write(*,*)'ncrys',ncrys
                              write(*,*)'nchild',nchild

                              STOP
                              END

C(((((((((((((((((((((((((((((((())))))))))))))))))))))))))))))

c     This subroutine is used to update all the variables of newly produced grains for
c     the computation of next time step.

     SUBROUTINE NEWGRAINS(IPARENT)
                              INCLUDE 'commons.tex'

                             DIMENSION   SMATGTEMP(3,3,MAXSLIP,MAXCRYS)
                              DIMENSION  TOTFTWDOM(MAXCRYS)
```

```
C     UPDATE NUMBER OF TOTAL OFFSPRING GRAINS, AND NEW OFFSRPING
GRAINS THAT WERE JUST
C     PRODUCED DURING THE CURRENT TIME STEP

      NCHILD=NCHILD+NTWINDOM(IPARENT)
                                  NNEWCHILD=NTWINDOM(IPARENT)

C     UPDATE VARIABLES FOR OFFSPRING GRAINS

      TOTFTWDOM(IPARENT)=ZERO

      DO 100 ICHILD=NCRYS+1,NCRYS+NNEWCHILD

                                                      IFLAG(ICHILD) = TWO

c     At the moment when offspring grain is generated, it inherits all the hardening
c     parameters from its parent grain.

        DO J=1,NSLIP
                                                      CRSST(J,ICHILD) =
CRSST(J,IPARENT)
                                  ENDDO

                                  SSAT(ICHILD) = SSAT(IPARENT)
                                  SSATBAS(ICHILD) = SSATBAS(IPARENT)
                                  SSATPYR(ICHILD) = SSATPYR(IPARENT)
                                  HSS(ICHILD) = HSS(IPARENT)
                                  HSSPYR(ICHILD) = HSSPYR(IPARENT)

c     Further twinning is not allowed in the offspring grain.

        DO K=1,NTWIN
                                  CRSSTWT(K,ICHILD) = TWINFINITY
                                  FTWSYS(K,ICHILD) = ZERO
                                  ENDDO

C     Set twin volume fraction of offspring grain to zero.

                                  FTWCRYST(ICHILD) = ZERO
                                  FTWTENT(ICHILD) = ZERO
                                  FTWCOMT(ICHILD) = ZERO

c     UPDATE FPTINV AND TBTMAT

                                  DO 10 K=1,3
                                  DO 10 L=1,3
```

```
                                FPTINVT(K,L,ICHILD)=FPTINVT(K,L,IPARENT)
10      CONTINUE

                                  DO 11 K=1,3
                                  DO 11 L=1,3
                                TBTMATT(K,L,ICHILD)=zero
11      CONTINUE

C     FIND WHAT TWIN SYSTEM IS THE NEW GRAIN GENERATED FROM

       ITWIN=NEWGRAIN(IPARENT,ICHILD-NCRYS)

C     FIND THE MAX VOLUME TWIN SYSTEM IN PARENT GRAIN

                                  ITWINMAX=NEWGRAINMAX(IPARENT)
                                  IPTR(ICHILD)=ITWIN

C UPDATE VOLUME FRACTION FOR CHILD GRAINS
C ASSIGN VOLUME FRACTION TO EACH NEW CHILD GRAIN (DOMINANT
TWIN SYSTEMS IN PARENT GRAIN)

       VFRAC(ICHILD)=FTWSYS(ITWIN,IPARENT)

C TOTAL VOLUME FRACTION OF THE NEW CHILD GRAINS (DOMINANT
TWIN SYSTEMS IN PARENT GRAIN)


TOTFTWDOM(IPARENT)=TOTFTWDOM(IPARENT)+VFRAC(ICHILD)

       IF(ITWIN.EQ.ITWINMAX) ICHILDMAX=ICHILD

c     UPDATE ORIENTATIONS FOR CHILD GRAINS BASED ON THE MATRIX-
TWIN ORIENTATION AT
C     INTERMEDIATE CONFIGURATION.

        DO 13 I=1,3
                                  DO 13 J=1,3

QMAT(I,J,ICHILD)=QMATTW(I,J,ITWIN,IPARENT)
13                                CONTINUE

                                   DO 12 I=1,NSLIP
                                                  DO 12 K=1,3
                                                  DO 12 L=1,3
                                SMATGTEMP(K,L,I,ICHILD)=0.0
                                   DO 12 M=1,3
```

```
SMATGTEMP(K,L,I,ICHILD)=SMATGTEMP(K,L,I,ICHILD)+
                       1          QMAT(K,M,ICHILD)*SMAT(M,L,I)
12      CONTINUE

                           DO 15 I=1,NSLIP
                                                DO 15 K=1,3
                                                DO 15 L=1,3
                          SMATG(K,L,I,ICHILD)=0.0
                             DO 15 M=1,3
                          SMATG(K,L,I,ICHILD)=SMATG(K,L,I,ICHILD)+
                          1
SMATGTEMP(K,M,I,ICHILD)*QMAT(L,M,ICHILD)
15      CONTINUE

        DO I=1,NSLIP
                          PMAT(1,I,ICHILD) = SMATG (1,1,I,ICHILD)
                          PMAT(2,I,ICHILD) = SMATG (2,2,I,ICHILD)
                          PMAT(3,I,ICHILD) = SMATG (3,3,I,ICHILD)
                          PMAT(6,I,ICHILD) = SMATG (1,2,I,ICHILD) + SMATG
(2,1,I,ICHILD)
                          PMAT(5,I,ICHILD) = SMATG (1,3,I,ICHILD) + SMATG
(3,1,I,ICHILD)
                          PMAT(4,I,ICHILD) = SMATG (3,2,I,ICHILD) + SMATG
(2,3,I,ICHILD)
                             ENDDO

100   continue

C      ASSIGN THE VOLUME FRACTION OF THOSE NON-DOMINANT TWINS to
the biggest
C      child grain IN ORDER TO KEEP THE SUM OF ALL VOLUME FRACTIONS
EQUAL TO ONE.

     VFRAC(ICHILDMAX)=FTWCRYST(IPARENT)-TOTFTWDOM(IPARENT)+
                       1                          VFRAC(ICHILDMAX)

C     UPDATE VARIABLES FOR PARENT GRAIN

                          IFLAG(IPARENT) = ONE
                          VFRAC(IPARENT)=ONE-FTWCRYST(IPARENT)

                          DO K=1,NTWIN
                            CRSSTWT(K,IPARENT) = TWINFINITY
                            FTWSYS(K,IPARENT) = ZERO
                          ENDDO
```

```
                                                    FTWCRYST(IPARENT) =
ZERO
                                    FTWTENT(IPARENT) = ZERO
                                    FTWCOMT(IPARENT) = ZERO


                                return
    end
```

APPENDIX E: FOURIER COEFFICIENTS NEEDED FOR COMPUTING TENSILE YIELD STRENGTH IN ANNEALED α-TITANIUM POLYCRYSTALS

1. The following Fourier coefficients (${}^{ii}_{y1}S^{\mu\nu}_{\ell}(q)$) are used to derive the effective tensile yield strength at upper bounds. For clarity, the coefficients listed below are only for discrete q in the increment of 0.2 in the range from 0 to 1.

$\overline{\sigma}'_{11}$

q	0	0.2	0.4	0.6	0.8	1
o11	141.618	157.61	165.41	165.402	157.618	141.623
211	-12.5359	-23.5985	-26.9394	-28.1348	-35.6095	-52.7122
212	68.0966	54.7292	48.0258	47.3532	47.7906	44.8791
411	-11.0759	-14.265	-20.4915	-20.2524	-18.8544	-30.9472
412	26.5782	35.6857	32.2489	32.0263	39.8086	44.388
413	-56.3424	-45.257	-41.3496	-41.6612	-39.8386	-32.7948
611	1.15793	-2.4654	-1.59114	-2.74949	-4.93833	-15.9762
612	8.51278	1.47909	1.98426	4.35439	7.75493	8.29341
613	-1.74256	-3.21924	-3.2693	-3.71497	-4.14044	-8.20128
614	18.7699	9.88179	5.90714	3.48031	3.83654	6.20294
621	1.74939	-0.16082	-0.58891	0.188158	2.86686	0.803877
622	4.39395	-0.56384	0.786215	-0.06659	-1.49423	-5.13978
623	-2.09704	-1.13344	-0.66484	-0.37197	0.011228	-2.44185
624	-3.4649	-2.96902	-0.05789	1.1295	-0.09572	2.30016
811	-0.43531	2.97438	3.67654	3.69121	2.3283	-6.4009
812	-9.34945	-7.00952	-5.43699	-5.29212	-5.01546	-6.14395
813	2.81155	7.03034	5.88927	5.63811	4.21766	6.17041
814	-12.5718	-6.72024	-6.46889	-6.58075	-7.73821	-8.83035
815	3.16685	7.11543	8.53951	8.65537	9.7379	8.2321
821	8.54859	-1.6592	-4.01599	-4.27905	-3.84977	-0.47225
822	-4.96327	2.92811	5.77197	5.99169	5.27914	4.53263
823	1.18355	-3.47736	-6.00535	-6.01492	-4.46879	-2.56658
824	3.50346	4.18884	6.54687	6.65687	4.54206	5.1785
825	-4.71122	-8.01112	-9.51371	-9.18456	-4.6557	8.89656
1011	0.060321	-1.28684	-2.06911	-2.75804	-5.26947	-3.20607
1012	0.504351	2.34716	3.10118	3.9639	6.05293	-1.89692
1013	1.67843	-3.12047	-3.32965	-4.06249	-5.3305	0.38502
1014	9.1046	5.82289	3.76848	4.13285	6.2445	8.07414
1015	-4.87076	-5.76453	-4.56937	-4.36771	-6.29378	-5.71565
1016	1.68266	10.3933	6.62522	5.33498	4.62007	1.08178
1021	12.5419	10.9717	5.72729	3.20485	1.36948	-0.44984
1022	-12.0216	-13.5619	-7.95956	-4.63789	-2.11316	-1.51539
1023	8.46097	9.503	7.62596	5.01491	2.85673	1.01096
1024	-6.641	-6.55219	-7.21021	-5.87138	-4.02663	-5.26247
1025	5.33518	5.12971	6.94304	7.64189	5.05939	3.9624
1026	-2.03266	-4.09268	-8.07493	-13.0335	-20.6185	-20.0772

1211	5.48733	4.914	5.23429	3.71876	-1.96914	-1.25753
1212	-9.64708	-8.41682	-7.38715	-5.33288	0.399456	-0.30469
1213	11.6007	8.36748	7.46114	5.6951	0.190712	-0.33176
1214	-10.6605	-10.0016	-7.58347	-6.2845	-1.98829	4.20308
1215	0.608617	7.72575	7.67968	7.25344	5.5774	-3.3012
1216	2.63038	-5.30165	-8.02665	-8.80865	-10.4996	-8.90875
1217	-1.48726	-0.59078	9.72076	12.9577	14.1624	16.4197
1221	-4.41632	-0.34846	0.055154	-0.38504	-1.74644	-0.28314
1222	8.38787	0.614272	-0.11675	0.501491	1.93259	1.67633
1223	-4.96757	-0.33427	0.254614	-0.37603	-1.60782	-0.3143
1224	1.70219	-0.90716	-0.29356	0.122183	1.61751	3.01589
1225	-1.7844	0.230354	0.277734	0.094194	0.008939	-0.63352
1226	2.1628	0.778281	-0.03168	-0.35626	-0.64594	1.23783
1227	-2.03869	-3.27459	-0.72883	0.280652	-0.60903	-10.7415
1231	0.010664	0.866874	0.753981	0.640946	0.529174	-0.70775
1232	-1.91953	-1.09248	-1.08079	-0.96309	-0.7184	-1.67235
1233	2.43229	1.12753	1.15419	1.13314	0.927184	0.930904
1234	-3.62485	-1.13622	-1.30972	-1.35766	-1.0639	1.45169
1235	-1.16598	1.27391	1.54361	1.56399	1.2693	-1.71292
1236	0.799579	-1.38801	-1.74615	-1.66358	-1.35753	-2.79057
1237	0.824416	1.46544	1.84648	1.96635	1.99907	2.93041

$\bar{\sigma}'_{22}$

q	**0**	**0.2**	**0.4**	**0.6**	**0.8**	**1**
o11	0.616081	-38.8288	-70.9622	-91.1092	-115.775	-139.665
211	84.2041	103.278	109.89	102.746	78.9479	52.3189
212	-49.0443	-12.1807	18.3806	30.9476	39.9754	44.6078
411	-50.2626	-28.5189	6.87808	27.2654	39.753	30.2781
412	-44.2827	-51.4806	-30.1548	-14.2498	18.5011	43.7543
413	58.4176	25.34	10.084	15.223	22.8651	31.7448
611	17.0284	17.8506	5.56216	7.88433	18.5423	15.164
612	-0.00407	7.05459	-1.17948	-6.70774	0.228963	7.89303
613	6.39012	2.21372	0.060591	8.47899	14.0335	8.1238
614	-12.3412	4.68093	4.70386	-0.60887	1.9854	5.4369
621	-1.49933	2.03295	1.27309	-3.20366	-0.01818	-0.65906
622	-9.01344	2.32386	-1.39232	4.0816	2.2051	-5.15674
623	-0.51606	-0.29428	1.79247	-2.25396	2.17869	2.21467
624	7.22786	2.19316	-5.26005	1.57742	-0.52434	2.34412
811	12.8019	7.40962	4.67017	2.65904	6.64245	6.02989
812	5.24529	0.298221	-4.31416	-3.43047	-4.84725	-6.20144
813	-9.06968	-11.6613	-0.31302	1.99236	-0.9253	-5.71891
814	8.81357	6.59998	5.39781	0.46198	-8.65499	-8.84164
815	-9.71534	-14.926	-13.2869	-14.044	-9.59446	-8.82883
821	-8.37077	13.4919	12.602	0.06664	-3.91351	0.479273
822	-4.77336	-18.195	-16.0368	-1.07314	3.41993	4.55854
823	4.71561	12.6759	11.3162	2.42973	0.813505	2.51371
824	-5.3532	-4.62513	-5.71985	-0.61692	1.89532	4.97431
825	7.33387	12.7355	7.84037	-14.0885	-20.7337	-8.75778
1011	6.31705	4.43408	3.17988	-0.36361	-2.15155	3.02026
1012	-0.661	-5.57756	-5.10203	0.191312	4.83794	-1.88021

1013	-6.95587	6.33725	5.21789	-0.0496	-2.60565	-0.27711
1014	-8.26274	-4.2362	-5.02864	-0.22715	-1.02453	7.85795
1015	9.86601	4.92834	4.84088	-0.92849	0.918022	4.95316
1016	0.512457	-15.1546	-7.06705	2.02007	3.829	0.44452
1021	-28.9676	-15.353	2.32697	4.53596	2.12999	0.358838
1022	24.3671	17.3517	-2.69626	-6.11834	-1.93021	-1.48075
1023	-11.8634	-8.67098	0.92107	5.13228	1.88837	-0.97008
1024	9.60582	6.22856	2.38995	-2.5264	-2.39698	-5.16134
1025	-7.05983	-6.00241	-7.566	-2.7437	-2.37521	-3.87803
1026	3.61624	7.72235	16.7154	15.2378	-5.40053	-19.6105
1211	4.61334	6.34337	6.04551	5.60147	-1.14618	1.13658
1212	-4.76111	-6.54383	-7.83757	-7.80995	-0.2952	-0.36977
1213	-6.68606	2.6187	5.68592	7.10034	1.85035	0.288375
1214	15.2687	9.41995	-1.58106	-5.48078	-4.74935	4.00261
1215	-4.25518	-14.3058	-3.7513	2.19603	10.5208	2.93726
1216	-3.85596	13.0264	10.4443	5.18286	-5.27273	-9.13543
1217	0.839192	-1.17117	-20.681	-22.2335	-19.6252	-16.0617
1221	-4.12933	-9.80518	-2.99901	2.13617	-0.68875	0.24446
1222	-2.46978	12.1415	3.95526	-2.80573	0.281275	1.61147
1223	1.05766	-7.43177	-2.87757	2.38272	0.562456	0.303644
1224	0.948695	4.13221	1.35968	-1.79277	-1.5854	2.92886
1225	1.61369	-1.8398	-0.8364	0.622077	1.03122	0.604202
1226	-3.53001	1.42032	1.3519	-0.49474	-0.32275	1.25878
1227	3.39027	3.28842	-3.67935	5.31946	17.7543	10.4373
1231	2.42054	0.953337	0.875905	0.770147	1.25018	0.706935
1232	-0.27089	-1.96001	-1.09314	-1.30776	-1.3619	-1.63978
1233	-1.00352	1.42237	0.520402	1.7797	1.37255	-0.90046
1234	6.02652	1.08723	0.828409	-2.258	-2.30291	1.38326
1235	-1.09386	-4.30125	-2.71059	2.16376	3.94582	1.51862
1236	-2.06488	4.30945	4.36469	-0.51242	-1.10384	-2.67378
1237	-1.88175	-4.33653	-4.53593	-3.17321	-4.07059	-2.94317

$\overline{\sigma}'_{33}$

q	**0**	**0.2**	**0.4**	**0.6**	**0.8**	**1**
o11	-139.669	-115.772	-91.112	-70.9589	-38.8347	0.607859
211	-64.789	-74.0765	-78.2107	-70.8227	-41.0806	0.390001
212	-23.0191	-48.3888	-73.5207	-85.9588	-95.5389	-97.4268
411	59.3352	42.1819	13.494	-6.78732	-20.7464	-0.42594
412	17.7705	16.3435	-1.9349	-17.9277	-58.4359	-88.8913
413	-2.58634	20.0131	31.5153	26.2706	16.1835	-0.53061
611	-15.9739	-14.2111	-3.24053	-4.37631	-13.0459	-0.18289
612	-8.66423	-9.52162	-1.86777	1.33534	-8.9522	-17.3903
613	-3.66479	1.67784	4.27464	-3.68888	-9.45376	-0.15703
614	-6.59282	-15.7751	-12.1547	-4.41512	-7.50487	-13.4952
621	-0.12164	-1.72823	-0.79477	2.85815	-3.00237	-0.0613
622	4.30639	-1.91778	0.775714	-3.79816	-0.59748	10.5434
623	2.42375	1.55956	-1.32349	2.41063	-2.16986	0.023366
624	-3.60747	0.947781	5.63697	-2.45463	0.383278	-4.89569
811	-12.7672	-10.5041	-8.40938	-6.40769	-9.00073	-0.24813

812	3.60656	6.59404	9.82406	8.81891	9.66659	11.4813
813	5.55058	4.5089	-5.64516	-7.74179	-3.40239	-0.1127
814	3.27079	0.22296	1.18196	6.21188	16.4691	17.7331
815	6.87374	7.88409	4.60062	5.2636	-0.19561	0.494496
821	-0.24824	-11.5443	-8.49525	4.13333	7.6197	-0.07658
822	9.39683	14.9268	10.1541	-4.82605	-8.58793	-9.2114
823	-5.56433	-9.00619	-5.23777	3.54392	3.68151	-0.0097
824	1.64257	0.276249	-0.85681	-6.053	-6.51641	-10.5347
825	-2.56149	-4.87387	1.5492	23.4384	25.884	0.184366
1011	-5.43603	-2.52476	-0.71933	3.13104	7.01127	-0.19406
1012	-0.74326	2.40822	1.46101	-4.18346	-10.4905	3.53758
1013	6.04669	-2.43243	-1.38372	4.19778	7.50283	-0.0876
1014	-0.22301	-1.75875	0.83364	-4.1119	-4.7557	-15.2569
1015	-5.32748	0.568324	0.02044	5.71342	5.52514	0.277059
1016	-2.04251	5.50423	0.334853	-8.21949	-9.7026	-2.90087
1021	16.0997	4.5925	-7.69437	-7.55252	-3.55931	0.057884
1022	-12.0868	-4.08073	10.1438	10.4689	4.09768	3.1396
1023	3.19844	-0.53008	-8.0384	-9.82609	-4.7102	0.030654
1024	-3.01817	0.024206	4.31908	7.99556	6.25294	10.2796
1025	1.89824	1.1107	1.10311	-4.35958	-2.38113	0.029632
1026	-1.5099	-3.59984	-9.14485	-3.0485	25.5259	40.1226
1211	-10.2115	-10.8961	-10.5501	-8.71331	2.87729	-0.09505
1212	14.0718	14.2196	14.1846	12.2691	-0.0653	0.619253
1213	-4.23943	-10.2025	-12.0799	-11.8696	-1.95251	-0.0074
1214	-5.49457	-0.36805	8.05006	10.7568	6.3883	-8.01376
1215	3.82029	7.34983	-2.75406	-8.31647	-15.4878	0.221401
1216	1.25142	-8.42717	-3.68227	2.29865	14.7019	17.0827
1217	0.50715	1.73663	12.5459	11.1124	6.72152	0.26593
1221	8.32919	9.86705	2.79614	-1.70171	2.42895	0.011399
1222	-5.62622	-12.2962	-3.64321	2.24188	-2.23768	-3.32236
1223	3.49491	7.3681	2.47036	-1.95397	1.08351	0.014675
1224	-2.28844	-3.03985	-0.95879	1.6303	0.014711	-5.98949
1225	-0.026	1.48603	0.518806	-0.70635	-1.02687	-0.01566
1226	1.39104	-2.16977	-1.34256	0.917108	1.14254	-2.1162
1227	-1.34048	0.002765	4.50691	-5.90367	-17.8345	-0.26469
1231	-2.38661	-1.80496	-1.65063	-1.46052	-1.84669	-0.07531
1232	2.14134	3.03406	2.20405	2.34071	2.1303	3.39173
1233	-1.43274	-2.58615	-1.7031	-2.96744	-2.28324	0.056859
1234	-2.20035	0.189972	0.505877	3.65155	3.35895	-2.96908
1235	2.08323	2.8497	1.14842	-3.75027	-5.34297	0.086694
1236	1.14663	-2.90617	-2.59224	2.20038	2.644	5.67488
1237	1.01209	2.80238	2.58356	1.1535	2.04607	0.027754

2. The following Fourier coefficients (${}^{ii}_{y1}S^{\mu\nu}_{\ell}$) are used to derive effective tensile yield strength at lower bounds. Note that 57 dimensions of Fourier series are utilized in this study.

o11	80.898
211	-12.4448
212	64.2941
411	4.48152
412	15.3136
413	24.789
611	-14.9654
612	22.0174
613	17.4939
614	11.7685
621	-12.981
622	5.12352
623	3.46237
624	16.1631
811	9.41137
812	-4.34313
813	10.8378
814	19.4422
815	5.70392
821	-10.4857
822	9.58618
823	-3.41547
824	1.80119
825	16.1563
1011	-1.44262
1012	5.09746
1013	5.7108
1014	7.53646
1015	11.9527
1016	5.6075
1021	-6.64412
1022	-15.0947
1023	-4.48909
1024	-1.35946
1025	2.78022
1026	7.63202
1211	-0.50288
1212	5.97375
1213	-1.72796
1214	9.9934
1215	4.02703
1216	7.09073
1217	4.3189

1221	-3.23716
1222	-3.88635
1223	-11.5769
1224	-5.10215
1225	-3.35437
1226	-0.30869
1227	9.25492
1231	4.20484
1232	-1.02318
1233	-1.33595
1234	-9.12944
1235	-6.62172
1236	-3.41543
1237	-1.36798

VITA

Name: Xianping Wu

Education:

- Ph.D. Department of Materials Science and Engineering, Drexel University, Philadelphia, PA 19104. 2006
- B.S. Department of Mechanical Engineering and Mechanics, University of Science and Technology of China, Hefei, Anhui, China. 2002

Experience:

- Graduate Research Assistant, Department of Materials Science and Engineering, Drexel University. 2002-2006
- Mentor for the research of undergraduates in a summer program (DREAM) funded by National Science Foundation (NSF), Drexel University. Summer, 2005.
- Teaching assistant: Mechanical Properties I, Department of Materials Science and Engineering, Drexel University. Spring, 2003-2004.

Professional Affiliations and Activities:

- ASM International and TMS. 2002 to present
- ASME. 2004 to present
- Material Advantage. 2005 to present
- President of Chinese Students and Scholars Association (CSSA), Drexel University. June 2004 – May 2005

Publications:

- X. Wu, S. R. Kalidindi, C. Necker and A. A. Salem, "Prediction of crystallographic texture evolution and anisotropic stress-strain curves during large plastic strains in α-titanium alloys using a Taylor-type crystal plasticity model", Acta Materialia 2006 (in press)
- X. Wu, G. Proust, M. Knezevic and S. R. Kalidindi, "Elastic-plastic property closures for hexagonal close-packed polycrystalline metals using first-order bounding theories", Acta Materialia 2006 (submitted)
- X. Wu, S. R. Kalidindi and R. D. Doherty, "Prediction of crystallographic texture evolution and anisotropic stress-strain curves in alpha-titanium using a Taylor-type crystal plasticity model", JOM, November 2004, v. 56, no. 11, p. 174

Presentations:

- Invited speaker at Los Alamos National Laboratory, January 2006
- MST 2005, Pittsburg, September 2005
- TMS Annual Meeting 2005, San Francisco, February 2005
- International Plasticity 2003, Quebec, July 2003